

**Disparities of topological states at multiple interconvertible domain walls**Zeyu Wu<sup>1</sup>,<sup>✉</sup> Xiaoshan Liu,<sup>1</sup> Guiqiang Liu,<sup>1,\*</sup> Shu Zong,<sup>1</sup> Jing Chen,<sup>2</sup> and Zhengqi Liu<sup>1,†</sup><sup>1</sup>*Jiangxi Provincial Key Laboratory of Advanced Electronic Materials and Devices, College of Physics and Communication Electronics, Jiangxi Normal University, Nanchang 330022, Jiangxi, China*<sup>2</sup>*College of Electronic and Optical Engineering, Nanjing University of Posts and Telecommunications, Nanjing 210023, China*

(Received 16 September 2023; revised 21 July 2024; accepted 23 July 2024; published 7 August 2024)

With the emergence of rich topological phases in artificial photonic crystals (PCs), numerous peculiar physical phenomena occur within domain walls (DWs) constructed by PCs with different topological phases. These phenomena include robust topological edge states (TESs), strongly localized topological corner states (TCSs), the quantum spin Hall effect, the quantum valley Hall effect, filling anomalies, and fractional charges at corners and edges. In this paper, we propose triangular lattice PCs composed of six triangle-shaped silicon rods to form two pairs of interconvertible DWs under two types of perturbations. We show that topological phase transitions occur with perturbations affecting 3 out of 6 rods. The first perturbation opens a band gap at the  $\Gamma$  point, supporting a pair of pseudospin helical edge states. The second perturbation opens another band gap at the  $K$  point, supporting valley edge states while preserving the initial topological band gap. We find that all designed topological PCs exhibit Wannier centers partially deviating from the center, causing different filling anomalies, thereby marking PCs with different topological indices corresponding to distinct higher-order topological phases. The results from mode charge distribution, calculated by integrating the local density of states (LDOS), are consistent with the Wannier center position analysis. By analyzing the LDOS under different boundary conditions at the corners and edges, we uncover significant disparities in the distribution of TES and TCS. Intriguingly, under certain conditions, the corner states can hybridize with edge states or even with bulk states. The rich topological physics presented not only provides insights into topological phases but also opens avenues for engineering topological states with potential applications.

DOI: [10.1103/PhysRevB.110.075407](https://doi.org/10.1103/PhysRevB.110.075407)**I. INTRODUCTION**

The concept of topological phases, derived initially from topological insulators in the field of condensed matter physics [1–3], has undergone extensive exploration in optical systems, such as photonic crystals (PCs) [2,4–17], waveguides [18–20], bound states in the continuum (BIC) [21–23], and even at disordered systems [23–26] as well as other nonoptical domains [27–33]. One notable outcome of this exploration is the emergence of robust topological edge states (TESs) governed by the bulk-edge correspondence principle. The TES exhibits robustness to defects, backscattering, and resistance to bending routes. This property unlocks potential applications, including optical splitters [34] and resonators [26]. Compared with conventional optical devices, topological PCs offer advantages such as increased bandwidth, reduced power consumption, and enhanced resistance to manufacturing imperfections [35–38]. Furthermore, authors of recent studies on TESs primarily categorize them into two types: pseudospin [15,39–41] and valley [42–44]. Extending the degrees of freedom of these TESs in optical systems facilitates innovative manipulation of light. While these systems offer robustness that is limited to a set of symmetry-preserving defects [9,45],

they still exhibit unidirectional boundary modes [46–48]. The design of topological PCs offers greater diversity than their counterparts in condensed matter physics, as different unit cell patterns can be fabricated artificially.

Higher-order photonic topological insulators have introduced the concept of topological corner states (TCSs), characterized by strong localization, and have garnered significant attention in research [49–53]. These topologically protected states manifest in lower dimensions. For example, in the realm of two-dimensional (2D) photonic systems, zero-dimensional TCSs [49,54–56] are a viable phenomenon. The TCS holds promise for various applications, including the development of low-threshold topological nanolasers [57] and the achievement of ultrahigh- $Q$  Fano resonance [58].

While corner states often indicate the presence of higher-order topology, they can also blend into the bulk bands [59,60]. Additionally, in numerous topological crystalline insulators, the discrepancy in spatial symmetry between the edges and the bulk leads to a failure in bulk-edge correspondence [35]. Researchers have recently shown that fractional mode charges at system boundaries or defects, a method to investigate the bulk topology without relying on these boundary states, can serve as excellent markers for studying topological phases [61–65]. Fractional mode charges are rigorously protected by both crystal symmetry and topology. Unless the system undergoes a topological phase transition, it remains unchanged. Therefore, they can serve as important signals

\*Contact author: [liugq@jxnu.edu.cn](mailto:liugq@jxnu.edu.cn)†Contact author: [zliu@jxnu.edu.cn](mailto:zliu@jxnu.edu.cn)

of topological crystalline phases, especially in topological photon systems where the symmetry at the bulk and edge differs.

In this paper, we study numerous higher-order topological phases and phase transitions in 2D PCs, which support fractional mode charges at the edge and corner boundaries, with a triangular lattice comprising unit cells consisting of six triangular-shaped silicon (Si) rods. To induce a transition from a trivial topological phase to a nontrivial one and a transition of diverse higher-order topological phases, we introduce two types of artificial perturbations, treated as perturbations, into a subset of Si rods within a unit cell. Two perturbations open two band gaps exhibiting distinct phase transitions, one of which hosts a pair of pseudospin helical edge states, and the other supports the valley edge states. Two types of perturbations enable the construction of two domain walls (DWs), where TESs and TCSs emerge. These perturbations provoke nontrivial distributions of the Berry curvature around  $\Gamma$  and  $K$  in the Brillouin zone. Additionally, the mode charge distribution—calculated by the integration of the local density of states (LDOS) over bulk bands—varies in response to alterations of higher-order topological phases. The fractional mode charge emerges at the corners and edges due to filling anomalies caused by the noncenter Wannier center [61–64]. We detect the quantum spin Hall effect (QSHE) by introducing circular polarization sources within the DW formed by combining a nontrivial topological PC with a trivial one. Numerous DWs, fabricated by PCs with different topological phases, are engineered to establish various boundary conditions. Notably, we observe gapped TESs and strongly localized TCSs exhibit varying distributions of frequencies in those DWs. By leveraging the QSHE realized on these DWs and photonic helicity, we designed optical logic gates. Our primary objective is to investigate the conditions and distinctions of topological states within these interchangeable DWs. Our discoveries present multiple interchangeable DWs within uncomplicated optical setups, emphasizing differences between TESs and TCSs. Although the immunity of TESs against effects that break the different symmetries of the phases (e.g., spin-flip processes in the QSHE, valley coupling terms in the valley phase, or certain crystallographic symmetry reductions) under the preservation of time-reversal symmetry is not well characterized in the literature at the moment, the TESs, characterized by their defect robustness and resistance to backscattering, along with the well-localized TCSs, are essential for optical applications. These findings unlock opportunities for tailoring topological states and exploring potential applications, including the implementation of TESs in topological optical splitters [34] and harnessing TCS for achieving ultrahigh- $Q$  Fano resonance [58].

This paper is structured as follows: In Sec. II, we present the PCs in different higher-order topological phases and their evolution processes. In Sec. III, we discuss various DWs composed of these different PCs. In Sec. IV, we explore the fractionalization of edges and corners under different boundary conditions based on the Wilson loop calculation method. In Sec. V, we investigate the robustness properties of these topological states. We conclude with a summary and outlook for future research in Sec. VI.

## II. TOPOLOGICAL PC

We consider the transverse magnetic (TM) modes within the designed photonic system, where out-of-plane  $H_z$  and in-plane  $E_x$  and  $E_y$  items are zero while other components remain finite. The dynamics of light are governed by the master equation derived from the Maxwell equation:

$$\vec{\nabla} \times \vec{\nabla} \times \vec{E}(\vec{r}) = \left( \frac{\omega^2}{c^2} \right) \varepsilon(\vec{r}) \vec{E}(\vec{r}), \quad (1)$$

where  $\varepsilon(\vec{r})$  of Si rods, being 12.11, are surrounded by air. The corresponding magnetic field can be obtained by the Faraday relation  $\vec{H}(\vec{r}) = -[i/\mu_0\omega] \vec{\nabla} \times \vec{E}(\vec{r})$ . The lattice vectors are denoted as  $\vec{a}_1$  and  $\vec{a}_2$ , where  $a_1 = a_2 = a = \sqrt{3}a_0$ . The unit cell contains six equilateral-triangle-shaped Si rods with a

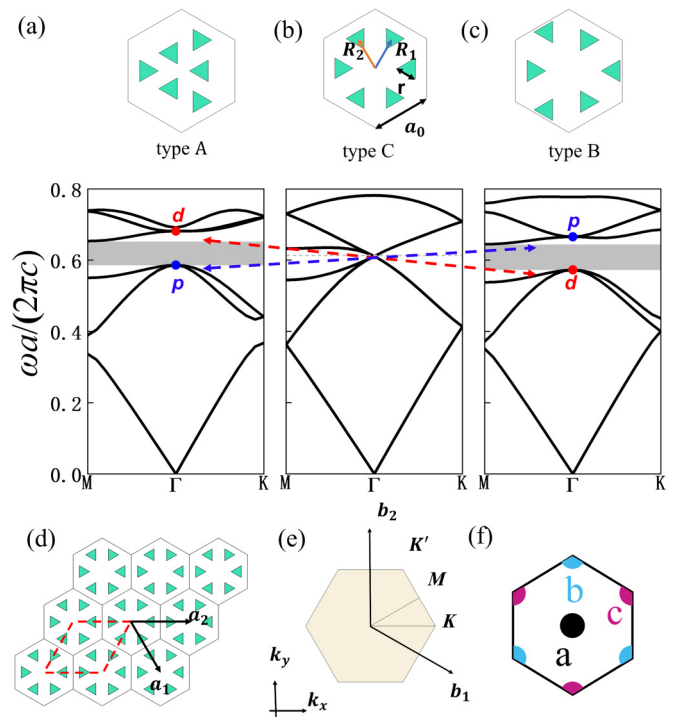


FIG. 1. Schematic of the unit cell of the two-dimensional (2D) photonic crystal (PC) and corresponding band diagrams. (a) The partially shrunken unit cell for  $m = 0.35$  is labeled type A and has a trivial band structure. (b) The unit cell for  $m = 1$  with a gapless band structure forms quadruple degeneracy at  $\omega a/(2\pi c) = 0.61$  at the  $\Gamma$  point is stamped type C. (c) The partially expanded unit cell for  $m = 1.4$  is marked as type B and exhibits nontrivial band structure. (d) Schematic of the 2D PC with  $\varepsilon = 12.11$ ,  $a = \sqrt{3}a_0 = 2580$  nm; red dashed rhomboid indicates another type of unit cell. (e) Brillouin zone of the proposed PC with points of high symmetry, where  $\vec{b}_1 = 2\pi/\sqrt{3}a(\sqrt{3}\vec{k}_x - \vec{k}_y)$  and  $\vec{b}_2 = 4\pi/\sqrt{3}a\vec{k}_y$ . (f) Maximal Wyckoff position for  $C_3$ -symmetric unit cells. The gray areas indicate band gaps opened at similar frequency widths between PCs in (a) and (b). As indicated by the dashed arrowed lines, the inversion of bands occurs between  $m = 0.35$  and 1.4 at the  $\Gamma$  point. The inversion involves an exchange between a pair of dipole modes ( $p_x$  and  $p_y$ ) and a pair of quadrupole modes ( $d_{xy}$  and  $d_{x^2-y^2}$ ).

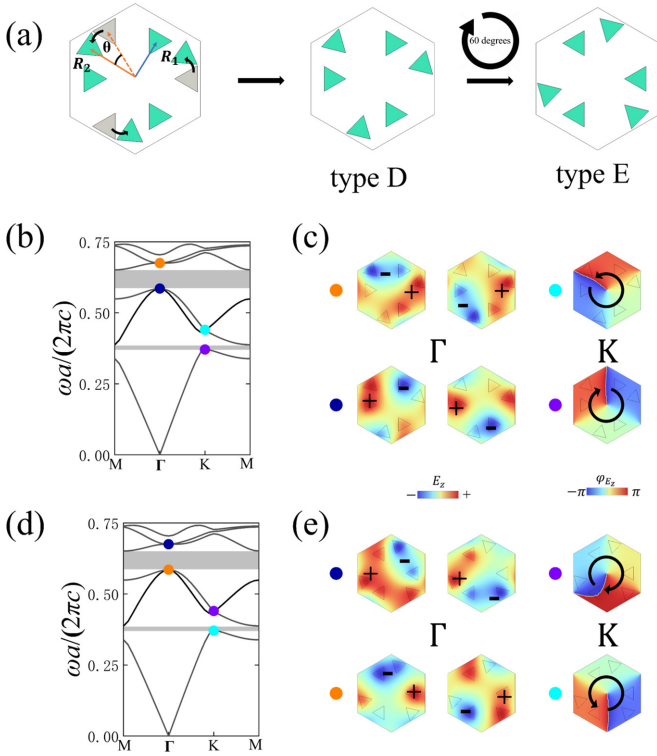


FIG. 2. (a) In the second perturbation, the perturbed triangle rod in type B rotates around its center by an angle  $\theta$  to evolve into type D, while all rods in type D are rotated by  $60^\circ$  to transform into type E. (b) and (d) Photonic band structures of types D and E at  $\theta = 17^\circ$ , where the first and second band gaps are marked with gray regions, and different colored dots indicate various eigenstate patterns at the  $\Gamma$  point and different phase winding properties at the  $K$  point. (c) and (e) Eigenstate distributions ( $E_z$ ) at the  $\Gamma$  point for types D and E, marked by pairs of differently colored dots, and phase diagrams of two eigenstates  $\varphi_{E_z}$  at the  $K$  point with opposite phase winding properties. The  $\pm$  indicates the positive and negative distribution of the eigenstate distributions  $E_z$ . Band inversion occurs simultaneously at the  $K$  and  $\Gamma$  points, supporting the coexistence of pseudospin and valley states.

length of  $r$ . As shown in Fig. 1(a), these Si rods are artificially divided into two groups, with two adjacent triangles belonging to different groups. The distance from the center of each rod in two groups to the center of the unit cell is  $R_1$  and  $R_2$ , respectively. In the absence of perturbations ( $R_1 = R_2 = a/3$ ), the photonic system with a triangular lattice containing six equivalent Si rods in each cell exhibits  $C_6$  crystal symmetry, which has two irreducible representations. Due to the double number of rods in the designed unit cell compared with the hexagonal lattice, such as graphene [66–68], with double degeneracy at points  $K$  and  $K'$  in the Brillouin zone, two Dirac cones are folded back to the  $\Gamma$  point, resulting in quadruple degeneracy, as shown in Fig. 1(b). At the degeneracy point, the  $E_z$  field carries  $p_x(p_y)$  and  $d_{xy}(d_{x^2-y^2})$  orbitals, as shown in Fig. 2(a), related to two pairs of pseudospin states, namely,  $p_+$ ,  $d_+$  for pseudospin-up and  $p_-$ ,  $d_-$  for pseudospin-down, where  $p_{\pm} = (p_x \pm ip_y)/\sqrt{2}$  and  $d_{\pm} = (d_{x^2-y^2} \pm id_{xy})/\sqrt{2}$ .

Here, we consider  $a = 2.58 \mu\text{m}$ ,  $r = na$ , and  $n = 0.35$ . In the case of  $R_1 = R_2 = a/3$ , six Si rods are equally split,

resulting in the designed PC resembling graphene, as shown in Fig. 1(b). The photonic band structure exhibits quadruple degeneracy at the  $\Gamma$  point around  $\omega a/(2\pi c) = 0.61$ , as displayed in Fig. 1(b). Figures 1(a) and 1(c) illustrate that one of the band gaps appears when the symmetry of the designed system changes. The proportionality coefficient  $m$  is introduced into the expressions for  $R_1$  and  $R_2$  to break the symmetry. The first group of Si rods remains fixed, namely,  $R_1 = a/3$ . The value of  $R_2$  is adjusted by  $m$  and can be expressed as  $a \times n/3 + a \times (1-n) \times m/3$ . There is no perturbation, meaning  $R_1 = R_2$  when  $m = 1$ ; the vertex of the adjusted triangle that is closest to the center of the unit cell coincides exactly with the center when  $m = 0$ . Meanwhile, the side length that is farthest from the center lines up precisely with the edge when the  $m = 1.5$ . It is evident that the symmetry of the system undergoes change from  $C_6$  to  $C_3$ , which gives rise to distinct distributions of special high-symmetry points (HSPs) within the real unit cell, namely, maximal Wyckoff positions when  $m$  deviates from 1. There are three distinct Wyckoff positions for  $C_3$ -symmetric unit cells, namely, a center ( $a$ ) and two corners of the unit cell ( $b$  and  $c$ ), as shown in Fig. 1(f). In various configurations of  $C_3$ -symmetric PCs, the Wannier centers demonstrate diverse distributions at these special positions. If located at the center point  $a$ , it aligns with the ionic center of the unit cell of an insulator, reflecting the electrical neutrality typical of traditional insulators in their trivial phase. However, the Wannier centers at corner  $b$  or  $c$ , which lead to the filling anomaly at corners and edges of PCs, are the primary drivers of the fractionalization of edge and corner charges. The fractionalization at varying edges and corners of PCs, which exhibit diverse higher-order topological phases corresponding to the distinct positions of the Wannier center located at different corners, will be discussed later.

Figures 1(a) and 1(b) show two opposite changes in two scenarios under the first type of perturbation: the enlargement of the distance of the selected triangle group ( $1 < m < 1.5$ ) and the shrinking ( $0 < m < 1$ ). Both perturbations of distance lead to a band gap between the third and fourth bands opening at the  $\Gamma$  point. To assess the impact of this perturbation on the gap, eigenfrequency as a function of proportionality coefficients  $m$  at the  $\Gamma$  point in the Brillouin zone is calculated, as illustrated in Fig. 3(a). It is evident that the perturbation induces a band gap scaling with the magnitude of deviation from  $m = 1$ , and there is a quasilinear relationship near  $m = 1$ . By comparing the change in eigenfrequency at the  $\Gamma$  point with  $m$ , we can select two perturbations with band gaps located at similar positions. When  $m = 0.35$  and 1.4, the two dispersion relations of the TM modes both have band gap in the frequency range around between  $\omega a/2\pi c = 0.653$  (75.9 THz) and  $\omega a/2\pi c = 0.586$  (68.09 THz). The gap opened for these specific perturbations is properly wider than most other perturbations, making them suitable for demonstrating the topological phase transition. The partly shrunken PC denoted as type A ( $m = 0.35$ ), and the partly expanded one, denoted as type B ( $m = 1.4$ ), possess similar band structures with the nearly identical band gap between the third and fourth photonic bands.

In the initial type of perturbation, where the system transitions from  $C_6$  to  $C_3$ , there is consideration to introduce the second type of perturbation to further disrupt its symmetry.

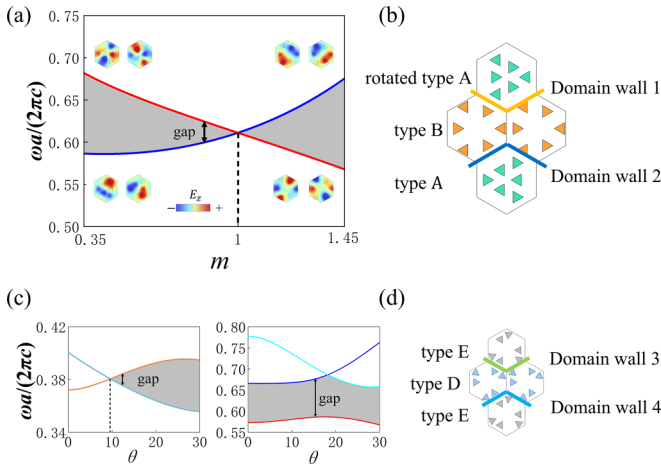


FIG. 3. (a) The eigenfrequency of a pair of  $p$  and  $d$  mode shifts with  $m$  at the  $\Gamma$  point. (b) Schematic of domain walls (DWs) composed of combinations of photonic crystals (PCs). The topological phase transition occurs with band inversion when  $m$  crosses 1, corresponding band gap, as marked by black arrow line, open, as shown in (a). DW1 comprises PCs of rotated types A and B, and the interface between types A and B produces DW2. (c) The left image shows how the eigenfrequency at the  $K$  and  $M$  points varies with the angle  $\theta$ , with the gap opening at approximately  $\theta = 9.5^\circ$ . The right image illustrates the evolution of the eigenfrequency at the  $\Gamma$  point with  $\theta$ , where the gap remains open throughout the entire range of  $\theta$ .

This second perturbation is specifically applied to type B PCs. From the first image of Fig. 2(a), it is observed that, under this perturbation, the triangle group, which has undergone the initial perturbation and has been expanded, rotates counterclockwise around the center of the cell by an angle  $\theta$ . It is evident that this perturbation still maintains the  $C_3$  symmetry of the system, preserving the maximal Wyckoff positions unchanged. However, it disrupts the mirror symmetry. Under this perturbation, a new gap opens between the first and second bands, while the gaps between the third and fourth bands—caused by the previous perturbation—remain unchanged. After experiencing this perturbation, the PC is designated as type D, and upon undergoing a rotationally flipped operation—rotating clockwise by  $60^\circ$ —it transitions to type E, as depicted in Fig. 2(a).

It is straightforward to infer that the band structures of types D and E are the same, as illustrated in Figs. 2(b) and 2(d). However, as depicted in Figs. 2(c) and 2(e), the eigenstate patterns of  $E_z$  at the  $\Gamma$  point are swapped between the two types of PCs with opposite phase winding properties at the  $K$  point, which indicates distinct higher-order topological phases. These changes not only result in the exchange of two degenerate points at the  $\Gamma$  point within the former band gap, leading to the emergence of two pairs of pseudospin states as previously discussed, but they also enable the realization of the valley Hall effect within the newly formed band gap due to the opposite phase-winding behaviors.

To clarify the impact of the second perturbation on the two band gaps, we calculated the evolution of characteristic frequencies at the  $K$ ,  $M$ , and  $\Gamma$  points as a function of the angle  $\theta$ . The results are shown in Fig. 3(c), where it is evident from the evolution of the eigenfrequencies at the  $\Gamma$  point that this

perturbation has a minimal effect on the band gap supporting pseudospin states, with the band gap essentially remaining constant at  $\omega a/2\pi c = 0.66$  and  $0.57$  throughout the changes in angle  $\theta$ . However, for the newly emerged band gap supporting valley states, it only opens when the angle  $\theta$  exceeds  $\sim 9.5^\circ$ . As seen from the band structure of type B in Fig. 1(a), the eigenfrequency at the  $K$  point on the first band initially exceeds that at the  $M$  point on the second band, but it gradually decreases with increasing  $\theta$ , while the eigenfrequency at the  $M$  point on the second band correspondingly rises.

To prove the topological phase difference between types A and B, the  $\mathbf{k} \cdot \mathbf{p}$  perturbation theory is applied to Maxwell's equations of 2D PCs. The effective Hamiltonian can be divided into two, denoted as

$$H(\vec{k}) = H_0 + H', \quad (2)$$

where  $H_0$  represents the Hamiltonian without perturbation and  $H'$  is designated as a perturbation term, denoted as  $\vec{k} \cdot \vec{p}$ , where  $\vec{k}$  is the wave vector, and the  $x$  component of the momentum operator  $p_x$  is defined as  $\partial/\partial x$  as well as  $p_y = \partial/\partial y$ . Here,  $H(\vec{k})$  can be rewritten under the basis  $[p_+, d_+, p_-, d_-]$  as [15]

$$H(\vec{k}) = \begin{pmatrix} H_+ & 0 \\ 0 & H_- \end{pmatrix}, \quad (3)$$

where  $H_\pm$  are summarized as

$$H_\pm = \begin{pmatrix} M + Bk^2 & Ak_\pm \\ A^*k_\pm & -M - Bk^2 \end{pmatrix}, \quad (4)$$

where  $A$  and  $B$  can be determined from the off-diagonal and diagonal terms of  $H'$  based on The  $\mathbf{k} \cdot \mathbf{p}$  perturbation theory,  $k_\pm = k_x \pm ik_y$ , and  $M$  is associated with the eigenvalues of  $H(0)$ , namely, the unperturbed term  $H_0$ , denoted as  $(\varepsilon_d - \varepsilon_p)/2$ . Here,  $\varepsilon_d$  and  $\varepsilon_p$  are the eigenfrequencies of  $E_z$  states carrying  $d$  and  $p$  orbits at the  $\Gamma$  point. The spin Chern number for two pseudospin states around the  $\Gamma$  point can be summarized as

$$C_\pm = \pm \frac{1}{2} [\text{sgn}(M) + \text{sgn}(B)], \quad (5)$$

where  $B$  stemming from the diagonal terms of the perturbed Hamiltonian is generally negative. It is noted that, if  $M > 0$ , namely,  $\varepsilon_d > \varepsilon_p$ , the spin Chern number  $C_\pm = 0$ , indicating the PC is in a trivial phase. Conversely, if  $M < 0$ , namely,  $\varepsilon_d < \varepsilon_p$ , the spin Chern number  $C_\pm = \pm 1$ , signifying that the PC is in a topological phase. The  $M$  serves as the critical factor for judging the topological phase of the PC. As  $M$  transitions from positive to negative, there is an inversion of the bands between the pair  $p$  and  $d$  modes, as shown in Fig. 3(a), leading to a shift from a trivial phase to a topological phase. The presence of this inversion results in the appearance of topological states.

Based on the comparison of the two pairs of modes at the  $\Gamma$  point between types A and B, along with the evolution of eigenfrequency at the  $\Gamma$  point with the  $m$  in Fig. 3(a), we observe that the eigenfrequency of a pair  $p$  mode is directly proportional to  $m$ . In contrast, the eigenfrequency of a pair  $d$  mode exhibits an inverse trend. These two frequencies intersect at the point  $m = 1$ , indicating the presence of different topological phases on either side of this point. In specific

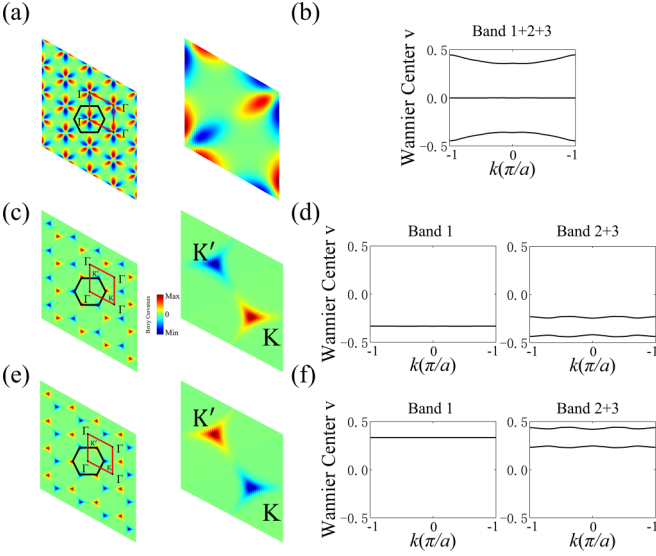


FIG. 4. (a) Berry curvature distribution for the first three bands of type B in the reciprocal space, with the left image showing the first Brillouin zone marked by a black hexagon, and the plaquette formed by  $\vec{b}_1$  and  $\vec{b}_2$  in Fig. 1(e) highlighted in red, where all four vertices are the  $\Gamma$  point. The left image displays the Berry curvature distribution over a Brillouin zone composed of a  $4 \times 4$  plaquette, and the right image is for a single plaquette. (b) Wannier band for the first three bands, which shows the characteristic Wilson loop of the photonic obstructed atomic limit. (c) and (d) Berry curvature distribution for the first band of types D and E in the reciprocal space, which shows opposite behaviors at  $K$  and  $K'$  points between the two types of photonic crystals (PCs). (e) and (f) Wannier band for the first band and the second and third bands, which shows nontrivial polarization.

terms, type A with  $m = 0.35$  is in the trivial phase with the spin Chern number  $C_{\pm} = 0$ , and type B is in the topological phase with  $C_{\pm} = \pm 1$ . To further verify the pair of spin Chern numbers for type B, we calculated the Berry curvature distribution and Wannier band for the first three bands of type B using a discretized calculation across the Brillouin zone, as illustrated in Figs. 4(a) and 4(b). The detailed calculations of these bands are discussed in Appendix A in the Supplement Material [69]. We found that the Berry curvature distribution around the  $\Gamma$  point forms a petal shape, regularly distributed around the  $\Gamma$  point with adjacent Berry curvatures being oppositely signed. At the  $\Gamma$  point itself, the value is zero due to the superposition of two opposite spin Chern numbers. From the nontrivial Wannier band, it is evident that the phase of type B is the photonic obstructed atomic limit (OAL), which differs from the trivial phase in which the Wannier centers are not located at the center of the unit cell but at its edges.

To prove that types D and E represent different higher-order topological phases, we calculated the topological invariants corresponding to the HSPs in the reciprocal space below their first band gap. We denote the HSP as  $\Pi$ , for  $C_3$  eigenvalues of  $\Pi$ , marked as  $\Pi_{(n)}$ , can only be  $\Pi_{(n)} = \exp[i2\pi(n-1)/3]$ , for  $n = 1, 2, 3$ . The topological invariants can be defined as  $[\Pi_{(n)}] = \#\Pi_{(n)} - \#\Gamma_{(n)}$  by referring to the  $\Gamma$  point, where  $\#\Pi_{(n)}$  [ $\#\Gamma_{(n)}$ ] is the number of bands below the band gap with  $C_3$  eigenvalues  $\Pi_{(n)}$  [ $\Gamma_{(n)}$ ]. However, some of

these invariants are not independent due to the time-reversal symmetry and the conservation of the number of bands below the band gap, resulting in redundancies among them [61,62]. By eliminating the redundant invariants, the indices  $\chi$  for  $C_3$ -symmetric PCs, which characterize the different topological classes, are determined by

$$\chi = ([K_1], [K_2]). \quad (6)$$

In trivial PCs, where band inversion does not occur, the eigenvalues  $\Pi_{(n)}$  at all the HSPs  $\Pi$  are identical, resulting in the invariants  $[\Pi_{(n)}] = 0$ . Conversely, a nonzero  $[\Pi_{(n)}]$  indicates the presence of a topological phase. We find that, for the first band of types D and E,  $\#\Gamma_1 = 1$  and  $\#\Gamma_2 = 0$ , the  $C_3$  eigenvalues at the  $K$  point for two types of PC can be determined by the phase profiles ( $\varphi_{E_z}$ ), illustrated in Fig. 2(c) and 2(e). Therefore, the topological indices are  $\chi = (-1, 0)$  for type D and  $\chi = (-1, 1)$  for type E.

The variations in bulk polarizations between types D and E indicate different topological classes. The polarization of the occupied bands, derived from the Wannier band, is specified as follows:

$$p_s = \frac{1}{N_k \sum_{j,k} v_s^j(k)}, \quad (7)$$

where  $s$  indicates the direction of projection of polarization along the lattice vector  $\mathbf{a}_s$ ,  $N_k$  represents the number of discretizations of  $k$ , and  $j$  denotes the index of the occupied bands. The polarization  $\mathbf{P} = (p_1 \mathbf{a}_1 + p_2 \mathbf{a}_2)$  and  $p_1 = p_2$  due to the  $C_3$  symmetry of the PCs we design in this paper. Wannier bands for the first band in types D and E for  $\theta = 17^\circ$ , as shown in Figs. 4(d) and 4(f), display corresponding polarizations with values of  $-\frac{1}{3}$  and  $\frac{1}{3}$ , respectively. This reflects that the Wannier center for the first band of type D is located at the maximal Wyckoff position  $c$ , whereas for type E, it is located at the maximal Wyckoff position  $b$ , as shown in Fig. 1(f). However, for the second and third bands, the value  $(p_1, p_2) = (-\frac{2}{3}, -\frac{2}{3})$  for type D and  $(\frac{2}{3}, \frac{2}{3})$  for type E. There are two Wannier centers present in two bands. One is at the maximal Wyckoff position  $b$ , and the other is at the maximal Wyckoff position  $a$ ; for type E, one is at the maximal Wyckoff position  $c$ , and the other is at the maximal Wyckoff position  $a$ . Interestingly, for the second band gap, summing the polarizations of the band below results in a total polarization of zero for both types D and E. This scenario is the same for type B, as illustrated in Fig. 4(b), where one Wannier band is at zero, and the other two are precisely opposite in sign. Therefore, the distribution of the three Wannier centers is not entirely concentrated at the center point of the unit cell. Only one is located at the center, while the other two are at different corners of the unit cell. The Wannier bands for type D at different values of  $\theta$  are displayed in Appendix A in the Supplemental Material [69]. They all have structures like the Wannier bands shown in Fig. 4(b).

### III. DWs

Types A and B with different topological phases can be used to construct the DW1. However, supposing that 1 of the 2 PCs, like type A, is rotated by  $60^\circ$ , the rod pattern at the edge between the two types of PCs changes. Figure 3(b) illustrates

two various DWs. DW2 (blue line) is formed by combining types A and B and can be turned into DW1 (yellow line) by rotation of type A, and DW2 can be changed back to DW1 by antirotation of type A. Types D and E, being in two different higher-order topological states, can also form two DWs based on their relative positions, as illustrated in Fig. 3(d). When type E is positioned above type D, the interface formed is DW3, marked by a green line. When the positions of types E and D are swapped, a new interface, DW4, is formed, labeled by a light blue line. The difference in rod pattern and topological phase between the four DWs leads to distinct behavior in the TES and TCS. Meanwhile, this difference can make the proposed PC suitable for various optical applications such as splitters [34] or PC heterostructures [77].

To demonstrate the difference between the first two DWs, the supercell with DW1 (DW2) comprising 10 unit cells of rotated type A (type A) and 10 unit cells of type B is built, marked as a yellow (blue) dashed line in Fig. 5(a). The projected band structures of supercells can be calculated by employing Floquet periodicity along the  $x$  direction and applying the scattering boundary condition along the  $y$  direction. Figure 5(b) displays the result of calculations. Notice that two DWs all exhibit gapped TESs within the band gap, and the evolution of the upper (lower) states of two DWs along the  $k_x$  direction is quite similar. In this case, the group velocities of two upper states, or lower ones, at two DWs have the same sign in plus or minus. However, the bandwidth for low- or high-frequency TESs at two DWs is different. As can be seen from Fig. 5(b), the gap between the two TESs varies, with the gap at DW2 being wider than at DW1, resulting in differences in the topological frequency windows for low-frequency (high-frequency) ranges between the two DWs. The variations in range and position of bandwidth at two interconvertible DWs can hold significant potential for optical applications such as optical splitters [34]. Given the presence of gapped TESs at the DWs, the existence of TCSs can be confirmed based on the bulk-edge-corner correspondence principle [49] that, if the eigenmodes of TESs at  $k_x = 0$  and  $\pi/a$  have different parity, the TCSs will emerge at specific frequencies within the band gap of the TESs. The distribution of  $E_z$  for the upper TESs at two DWs is displayed in Fig. 5(c). The parity between  $k_x \rightarrow 0+$  and  $k_x = \pi/a$  at two DWs is opposite. This discrepancy in parity reflects the presence of TCSs at both DWs [19,49]. To investigate the QSHE, the local chirality (or directionality) map is introduced, characterized by the Stokes parameters derived from the magnetic field [77,78], namely,  $D = S_3/S_0$ , where  $S_0 = |H_x|^2 + |H_y|^2$  and  $S_3 = -2\text{im}[H_x \times \text{conj}(H_y)]$ . Like the ellipticity, the sign of  $D$  distinguishes the chirality. Both chirality maps of two TESs around the  $\Gamma$  point are presented in Fig. 5(d) and exhibit non-trivial distribution with positive and negative chiralities. The  $D$  of upper TESs is nearly opposite to the lower ones, which is related to their opposite group velocities. The opposite behavior in  $D$  and power flow between the two TESs reveals that the upward-facing triangle TES exhibits a pseudospin polarization opposite to the one marked with a downward-facing triangle.

To illustrate the coexistence of pseudospin and valley states between the other two DWs, supercells with DW3 (DW4) are constructed, comprising 10 unit cells of type E (type D)

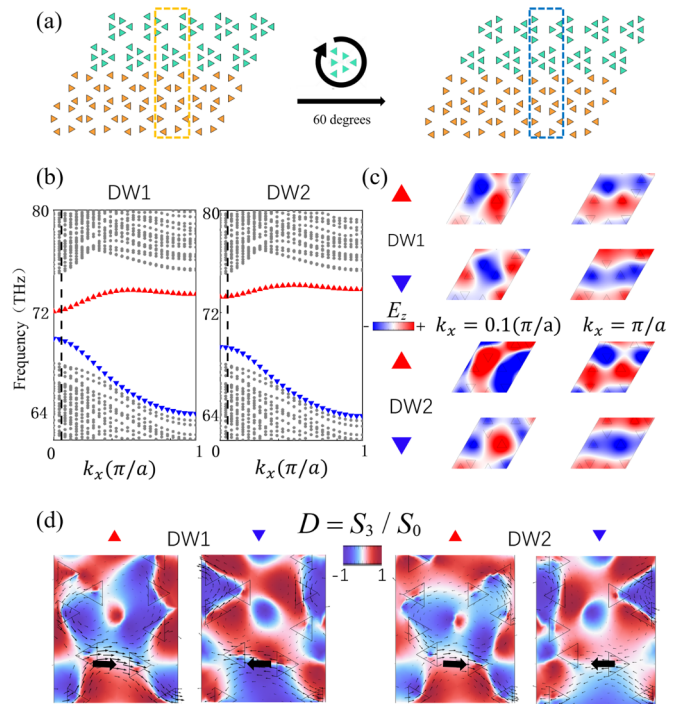


FIG. 5. (a) Schematic of the photonic crystals (PCs) with the first two interconvertible domain walls (DWs). DW1 can be transformed into DW2 through a  $60^\circ$  clockwise rotation. The yellow dashed rectangle is a supercell with periodic conditions in the  $y$  directions and a lattice constant in width, used to calculate the projected band with DW1, and the blue dashed line is to obtain the projected band with DW2. (b) Both projected bands of the two DWs exhibit two topological edge states (TESs). The direction of the triangles represents pseudospin polarization, with colors indicating the group velocity near the  $\Gamma$  point at  $k_x = 0.05 \times \pi/a$ ; red represents positive velocity, and blue represents negative. (c) Distribution of  $E_z$  around two DWs. The  $E_z$  fields around the  $\Gamma$  point at  $k_x = 0.05 \times \pi/a$  and  $k_x = \pi/a$  are amplified and rotated to investigate the change of parity. (d) Chirality (directionality) map around DWs at  $k_x = 0.05 \times \pi/a$ . The black arrow represents the power flow located at the region around  $D = 0$ . The chirality map and the direction of power flow exhibit opposite characteristics for the upper and lower modes within the same DW, while the upper or lower TESs at different DWs are similar. When  $k_x < 0$ , the chirality map and the direction are opposite to that of  $|k_x|$ . Additionally, the fact that the chirality map and direction of lower (upper) TESs at  $-|k_x|$  is like that of upper (lower) TESs at  $|k_x|$  results in the same pseudospin polarization between the left side ( $k_x < 0$ ) of lower (upper) TESs and the right side ( $k_x > 0$ ) of upper (lower) TESs, contributing to the quantum spin Hall effect (QSHE).

in the upper part and 10 unit cells of type D (type E) in the lower part. These configurations are indicated by cyan (purple) dashed lines in Fig. 6(a). The projected band structures of these supercells can be calculated by employing Floquet periodicity along the  $x$  direction and applying scattering boundary conditions along the  $y$  direction. Figures 6(b) and 6(d) show the band structures around the pseudospin band gap and valley band gap for the case of  $\theta = 17^\circ$ , respectively. The gray areas represent bulk states, and both band gaps contain two gapped TESs of pseudospin-up (marked by upward red triangles) and pseudospin-down (marked by

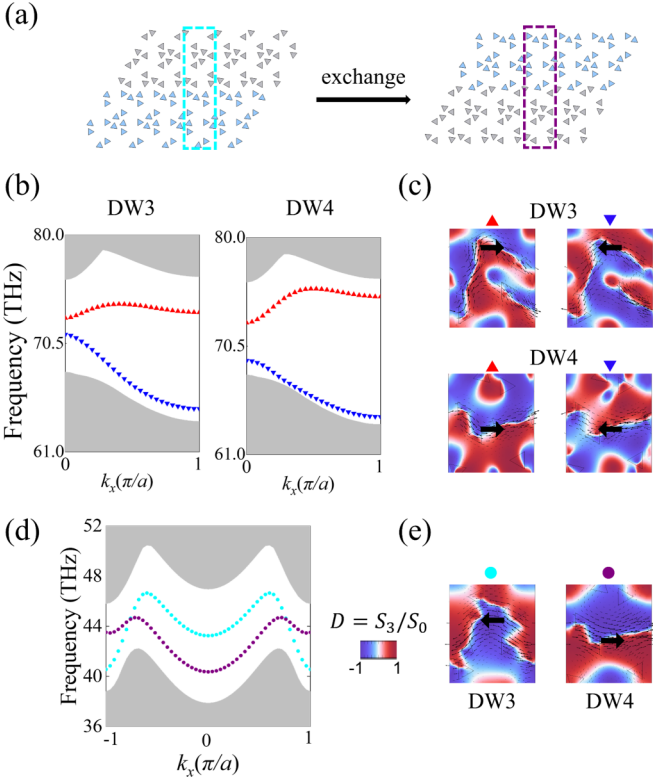


FIG. 6. (a) Schematic of the photonic crystals (PCs) featuring two other interconvertible domain walls (DWs). DW3 can be transformed into DW4 by exchanging the positions of types D and E. The cyan dashed rectangle denotes a supercell with periodic conditions in the  $y$  direction and a lattice constant in width, used to calculate the projected band for the supercell marked with DW3, while the purple dashed line is utilized to determine the projected band for the supercell with DW4. (b) Projected bands of two supercells around pseudospin band gap. Both feature two gaped topological edge states (TESs) with opposite pseudospin polarization. (c) Chirality maps of two supercells around DWs. The black arrow represents the Poynting flow. (d) Projected bands of two supercells around the valley band gap. The cyan dotted line indicates the valley edge states of the supercell containing DW3, while the purple dotted line signifies the valley edge states of the supercell with DW4. (e) Chirality maps of two supercells around DWs at the  $K$  point, along with the opposite Poynting flow between two DWs.

downward blue triangles). However, the bandwidths of the two TESs on DW3 and DW4 also differ. In Appendix B in the Supplemental Material [69], the projected band structures of supercells with DW3 (DW4) under different  $\theta$ 's were considered, revealing that  $\theta$  significantly affects the two pseudospin TESs on both DWs. Nevertheless, as discussed in Sec. II, for different  $\theta$ 's of type D (or type E), they are in the same higher-order topological phase. This indicates that symmetry at the edges of higher-order photonic topological insulators needs careful consideration. Both local chirality maps with the power flow of two TESs around the  $\Gamma$  point are presented in Fig. 6(c). Clearly, the behavior in chirality maps and power flow of two TESs on the same DW is opposite, reflecting the opposite pseudospin polarization of the two TESs. Unlike the first two DWs, the chirality map distribution on the current two DWs is very different. These differences

allow for the design of efficient optical logic gates, which is discussed in detail in Appendix B in the Supplemental Material [69]. Only a TES appears on the valley band gaps, as illustrated in Fig. 6(d), with the cyan and purple dotted lines representing valley TESs at DW3 and DW4, respectively. Both local chirality maps with the power flow of two TESs around the  $K$  point ( $k_x = \frac{2}{3} \times \pi/a$ ) are presented in Fig. 6(e), and at the  $K'$  point ( $k_x = -\frac{2}{3} \times \pi/a$ ), the chirality maps and power flow of TESs on both DWs are also opposite to those at the  $K$  point, reflecting the quantum valley Hall effect (QVHE). The distribution of chirality maps of TESs at the  $K$  point on both DWs is also different, and the directions of power flow are exactly opposite. This also indicates that boundaries have a significant impact on the QVHE system.

We discussed the cases where types D and E have the same  $\theta$ . Figure 7 shows the evolution of the gap between two pseudospin TESs in 225 different conditions for  $\theta$  ranging from  $9^\circ$  to  $23^\circ$ . Interestingly, these 225 cases are represented as a  $15 \times 15$  matrix, where the columns represent  $\theta$  in the upper part of the supercells, the rows represent  $\theta$  in the lower part of the supercells, and the size of the matrix elements is determined by the size and color of the square blocks within the grid. In both supercells with DW3 and those with DW4, the matrix is the symmetric matrix, and these two matrices can be approximately viewed as inverse diagonal flips of each other. Observing the evolution of the gap, in certain specific  $\theta$  values, the two gapped TESs become gapless. From the diagonal data, this occurs  $\sim 19^\circ$  for DW3 and  $\sim 13^\circ$  for DW4. In matrix elements where the gap is very small, the symmetry at the boundaries formed by two different domains is relatively high, illustrating that symmetry at edges has a significant impact on the distribution of TESs.

#### IV. FRACTIONAL CHANGE AND FILLING ANOMALY

The filling anomaly, which may manifest at corners and edges in topological PCs where a corner is formed by the intersection of two edges, is a critical feature in their electronic counterparts. This filling anomaly is central to the behavior of higher-order topological insulators (HOTIs), where there is an imbalance in the overall charge within the subspace of occupied bands. This phenomenon occurs due to a mismatch between the Wannier centers of the occupied bands and the atomic positions in HOTIs. In the topological photonic system, a similar mismatch can also occur, as discussed in Sec. II, where the Wannier center deviates from the center of the unit cell under different perturbations. This mismatch can lead to a loss of charge neutrality at the edges and corners, potentially resulting in fractional charges at these boundaries. Although photons are neutral particles, the fractional charge can be derived from the LDOS. Moreover, different topological phases can significantly affect the LDOS, leading to noticeable changes in the fractional charge at corners and edges obtained by integrating over the LDOS. These changes can be considered significant alterations in light-matter interactions and optoelectronic properties during topological transitions. In this section, we will discuss such changes. Using the LDOS, we can obtain the mode charge of each unit cell within a supercell. The mode charge of the  $i$ th unit cell is

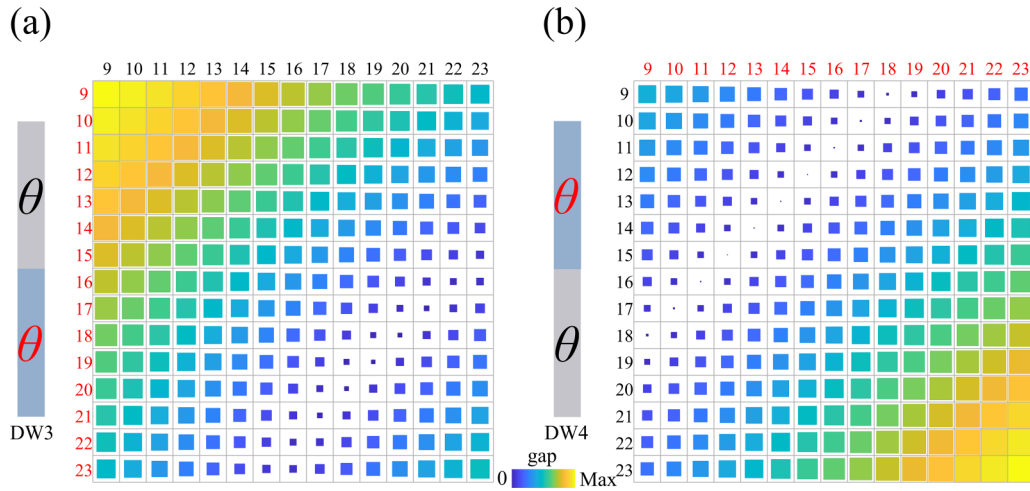


FIG. 7. (a) The gap between two pseudospin topological edge states (TESs) of supercells with DW3 under various configurations. The gray domain represents 10 unit cells of type E for  $\theta$  marked in black. The blue domain corresponds to 10 unit cells of type D for  $\theta$  marked in red. A  $15 \times 15$  grid forms 225 supercells with DW3, each representing different configurations. The vertical coordinates indicate  $\theta$  of type D, marked in corresponding colors, while the horizontal coordinates show  $\theta$  of type E, marked similarly. The size of the gap is denoted by the color and size of the square blocks within each grid; larger blocks correspond to larger gaps. (b) The gap between two pseudospin TESs in a supercell with DW4, formed after swapping positions between types D and E under various configurations.

given by [63,64]

$$C_i = \int_0^{f_{\text{gap}}} \int \rho_i(f, \mathbf{r}) df d\mathbf{r}, \quad (8)$$

where  $f_{\text{gap}}$  refers to a frequency below the band gap of concern, and  $\rho_i(f, \mathbf{r})$  is the photonic LDOS of the  $i$ th unit cell, which varies depending on the frequency  $f$  and the location  $\mathbf{r}$  of the  $i$ th unit cell. The mode charge  $C_i$  can be determined by the integration over real space within the  $i$ th unit cell and the bulk frequency. The charge measures the number of photonic modes from the  $i$ th unit cell that contribute to the valence band bulk states, analogous to the electronic charge that fills the valence band in their electronic counterparts. The photonic LDOS  $\rho_i(f, \mathbf{r})$  is discussed in detail in Appendix C in the Supplemental Material [69]. The total mode charge, obtained from the summation across all unit cells, exhibits robustness and only changes as the system undergoes a topological transition. Moreover, this change is abrupt if observed in an infinite system. This robustness of the changes is discussed in detail in Appendix D in the Supplemental Material [69].

To measure the fractionalization at the edge and corner, we first construct triangular supercells composed solely of one type of topological PC and surrounded by a perfect electric conductor (PEC). This configuration allows us to independently study the fractional charge at the edge and corner of topological supercells that are in different higher-order topological phases. To accomplish this, we constructed large triangular supercells composed entirely of type D units, with each side containing 12 unit cells, totaling 78 unit cells in the supercell. The structural diagram is shown in Fig. 8(a), where each blue hexagon represents a unit cell of type D for  $\theta = 17^\circ$ , and the spaces between each hexagon are intentionally left to clearly identify the specific location of each unit cell within the large triangular supercells. Each unit cell in the supercells is tightly packed without any gaps. From the structural diagram, we can clearly identify the unit cells situated at corners,

edges, or within the bulk. Notably, the 3 unit cells at the three vertices of the large triangular supercells are at corners; the remaining 10 unit cells on each side, excluding the vertices, are on the edges; and the rest are within the bulk. To study the distribution differences of the LDOS under different boundary conditions, we selected 1 unit cell each from those situated at the corner, edge, and bulk. We marked these selected unit cells with stars in three different colors: black for the bulk, red for the edge, and blue for the corner. The LDOS marked with corresponding color stars is displayed alongside the structural diagram. To observe the global changes in LDOS and between the two band gaps, three ranges are provided, as shown in Fig. 8(a). It was found that the LDOS distribution in the bulk unit cell corresponds exactly to the band distribution range of type D shown in Fig. 2(b), where two gaps are clearly visible in the LDOS. For the unit cells at the corner and edge, there is a significant reduction in the LDOS of bulk states, with varying degrees of reduction, reflecting the mismatch in charge between the bulk and at the edge and corner, i.e., filling anomaly. In the eigenstate spectrum next to the LDOS, we observed that there are 30 edge states within the pseudospin band gap, which exactly matches the number of unit cells at the boundaries. However, there are a total of six corner states, corresponding to three corner unit cells. The distribution of the LDOS at the corners and edges corresponds perfectly to the eigenstate spectrum. Interestingly, in the valley band gap, we did not observe the existence of a TES or TCS, which demonstrates the failure in bulk-edge correspondence mentioned in the introduction. However, their LDOSs within the range of the first band is significantly different from that of unit cells in the bulk. Figure 8(b) shows the structural diagram, LDOS, and eigenstate spectrum for type E at  $\theta = 17^\circ$ . It is evident that the LDOS distribution of the unit cell within the bulk is the same as for type D, yet changes occur at the corners and edges. Looking at the eigenstate spectrum at the pseudospin band gap, the edge states are more widely distributed,

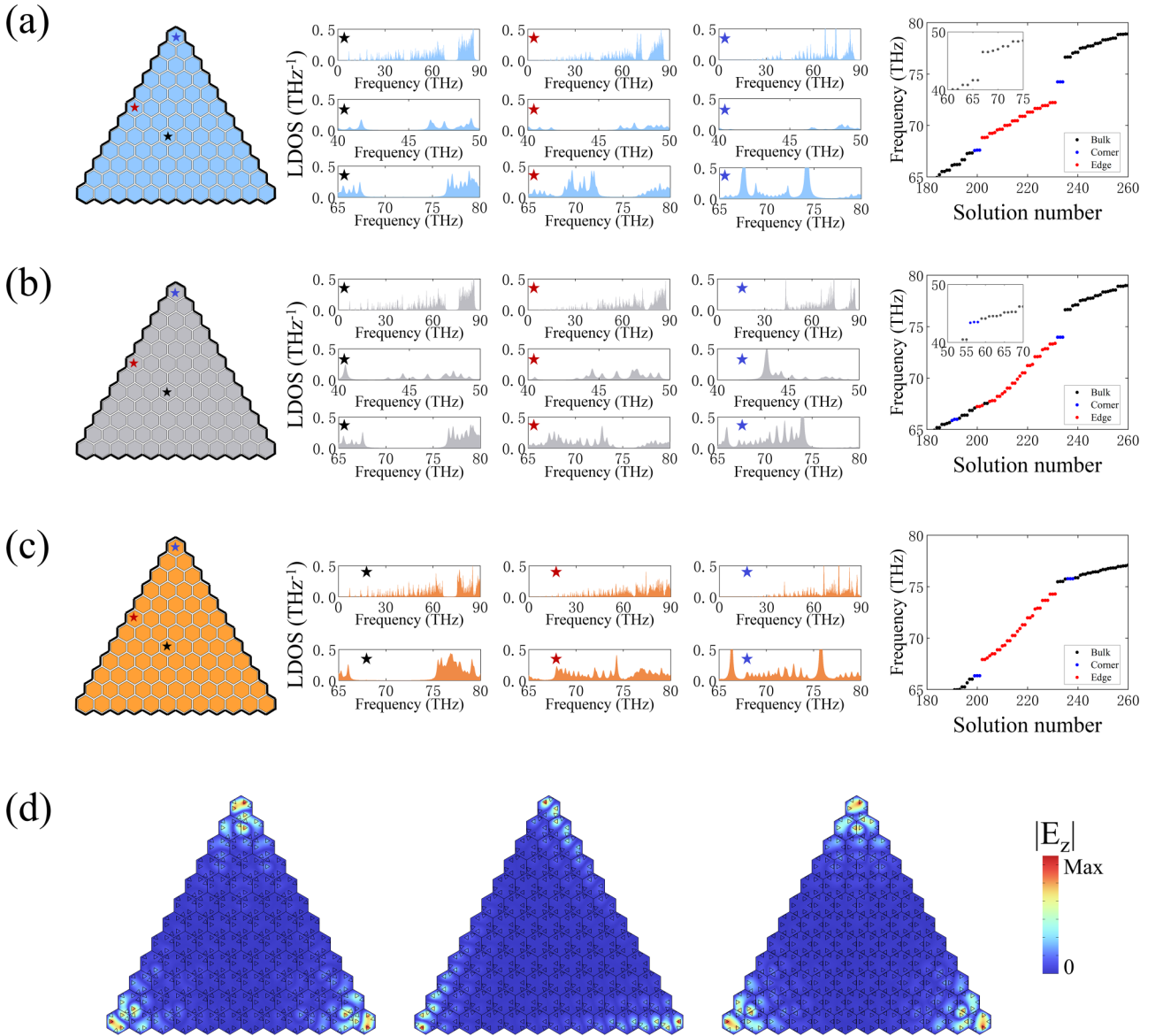


FIG. 8. (a) Schematic illustration of the large triangular supercells comprised of 78 unit cells of type D for  $\theta = 17^\circ$ , enclosed by perfect electric conductor (PEC) boundaries marked with a bold black line. Unit cells at different boundaries are indicated by stars in three colors: black for bulk, red for edge, and blue for corner. To the right of the schematic illustration are the photonic local densities of states (LDOSs) within these unit cells, marked by stars of corresponding colors. The photonic LDOSs are segmented into different regions. The first row spans from 0 to 90 THz, which includes the pseudospin band gap and the valley band gap. The second is between 40 and 50 THz, covering just the valley band gap. The third spans from 65 to 80 THz, encompassing the pseudospin band gap. Eigenspectra for type D are positioned to the right of the photonic LDOSs. Different states are marked by dots of the same colors, with black dots representing bulk states, red dots for edge states, and blue dots for corner states. Like the classification of photonic LDOSs, the ranges of the eigenstate spectrum match those of the LDOS with the lower-frequency eigenstate spectrum embedded within the higher one. (b) and (c) Schematic illustration of the large triangular supercells of types E and B. Similarly, stars and dots in the described colors represent corresponding photonic LDOSs and states. (d) Calculated electric field ( $E_z$ ) pattern for the corner state in the eigenstate spectrum, shown sequentially for types D, E, and B.

and three low-frequency corner states even lie within the bulk band and the lower-frequency bulk states. The phenomenon of bulk-edge-corner hybridization in topological states has been widely studied in recent research through the analysis of the LDOS [63,65,79]. In some cases, corner states within the bulk band can be seen as BIC [54,80]. This is because TCSs somewhere in the spectrum—whether within the bulk band (or edge bands) or the band gap—exhibit robustness, as evidenced by a prominent peak in the LDOS at the corners of type E

within the bulk band range. In the valley band gap, unlike type D, there is the presence of TCSs, as evidenced by the LDOS and eigenstate spectrum. As discussed in Appendix E in the Supplemental Material [69], we explored the evolution of the LDOS for types D and E at corners and edges under varying  $\theta$ . It was found that, as  $\theta$  increases, the peaks representing TCSs in both types tend to converge and undergo a redshift. For type E, the corner states either hybridize with the edge states or with the bulk states. The LDOS for type B, which

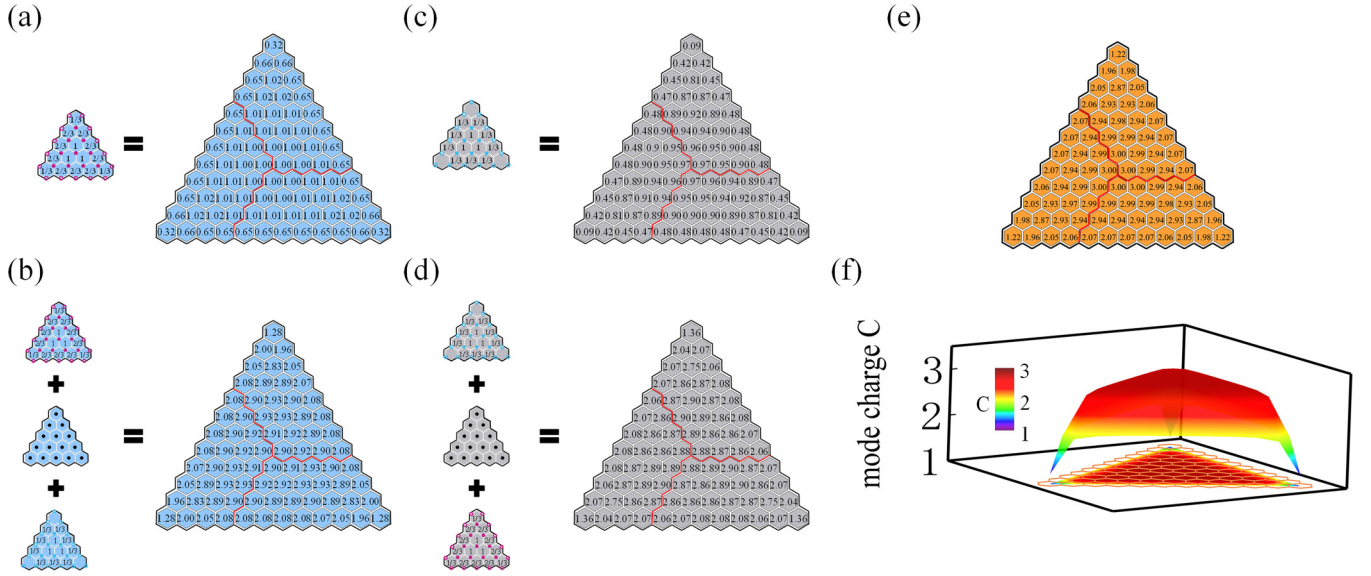


FIG. 9. Mode charge distribution and Wannier centers of topological photonic crystals with various topological phases. (a) Simplified schematic distribution of Wannier centers for type D below the valley band gap and a distribution map of the mode charge  $C$  for each unit cell below the valley band gap in large triangular supercells comprised 78 unit cells of type D for  $\theta = 17^\circ$ , enclosed by perfect electric conductor (PEC) boundaries marked with a bold black line. (b) Simplified distributions of the three different Wannier centers for type D corresponding to the three bands below the pseudospin band gap, along with the distribution map of the mode charge  $C$  for each unit cell in large triangular supercells. (c) Simplified schematic distribution of Wannier centers for type E below the valley band gap and a distribution map of the mode charge  $C$  for each unit cell below the valley band gap in large triangular supercells configured identically to (a). (d) Simplified schematic distribution of Wannier centers for type E below the pseudospin band gap, along with the distribution map of the mode charge  $C$  in large triangular supercells. (e) The distribution map of the mode charge  $C$  below the valley band gap in large triangular supercells of type B. (f) The three-dimensional (3D) rendering in (e) with a two-dimensional (2D) projection at the base. Since the unit cells exhibit  $C_3$  symmetry, these large triangular supercells can be divided into three equivalent areas using red lines. In each area, the distribution map of the mode charge  $C$  is identical.

has the same number of corner and edge states, is displayed in Fig. 8(c). The electric field distribution of the corner states in the three supercells is located at their three vertices, as shown in Fig. 8(d).

According to Eq. (8), the mode charge within each unit cell in large triangular supercells can be calculated. Figures 9(a) and 9(c) show the distribution of mode charge within the range of the first band for supercells of types D and E, respectively. From Sec. II, we know that the Wannier center for the bulk band below the valley band gap (i.e., the first band) of type D is located at the maximal Wyckoff position  $c$ , marked in purple, whereas for type E, it is at the maximal Wyckoff position  $b$ , marked in light blue, based on their distinct nontrivial polarization and Berry curvature distributions. The respective Wannier configurations in the supercell are displayed on the left side of the mode charge distribution in a simplified schematic diagram with differently colored dots, where solid dots represent bulk electrons in their electronic counterparts, and hollow dots represent boundary electrons for  $C_3$ -symmetry breaking. Bulk unit cells are always neutral, and charges at the edge and corner unit cells are indicated mod 1 after removing the symmetry-breaking boundary electrons. The configuration of bulk Wannier centers largely matches the mode charge distribution obtained through integrating the LDOS. A crucial distinction emerges between types D and

E, which are in different higher-order topological phases; Wannier centers at the maximal Wyckoff position  $c$  have a fractional corner charge of  $\frac{1}{3}$  and a fractional edge charge of  $\frac{2}{3}$ , whereas those at the maximal Wyckoff position  $b$  in type E display no expected fractional corner charge and a fractional edge charge of  $\frac{1}{3}$ . The mode charge within the range of the first three bands for supercells of types D and E, along with their corresponding Wannier configurations, are shown in Figs. 9(b) and 9(d). Within this range, both configurations have three Wannier centers. For type D, these centers are located at the maximal Wyckoff positions  $c$ ,  $a$ , and  $b$ ; for type E, they are at positions  $b$ ,  $a$ , and  $c$ . Ultimately, the superposition results in nearly identical mode charge distributions with a fractional corner charge of  $\frac{4}{3}$  (mod 1 results in  $\frac{1}{3}$ ) and an edge charge of 2 (mod 1 results in 0). The Wannier configuration for type B is consistent with that of types D and E, also featuring three Wannier centers below the pseudospin band gap. However, the three energy bands corresponding to the three Wannier centers at positions  $a$ ,  $b$ , and  $c$  differ. The mode charge distribution is shown in Figs. 9(e) and 9(f). For the three topological PCs, the mode charge distribution, whether below the valley band gap or the pseudospin band gap, can be divided into three equivalent parts due to the  $C_3$  symmetry of types B, D, and E. This division, indicated by red lines, significantly simplifies the computational effort needed to

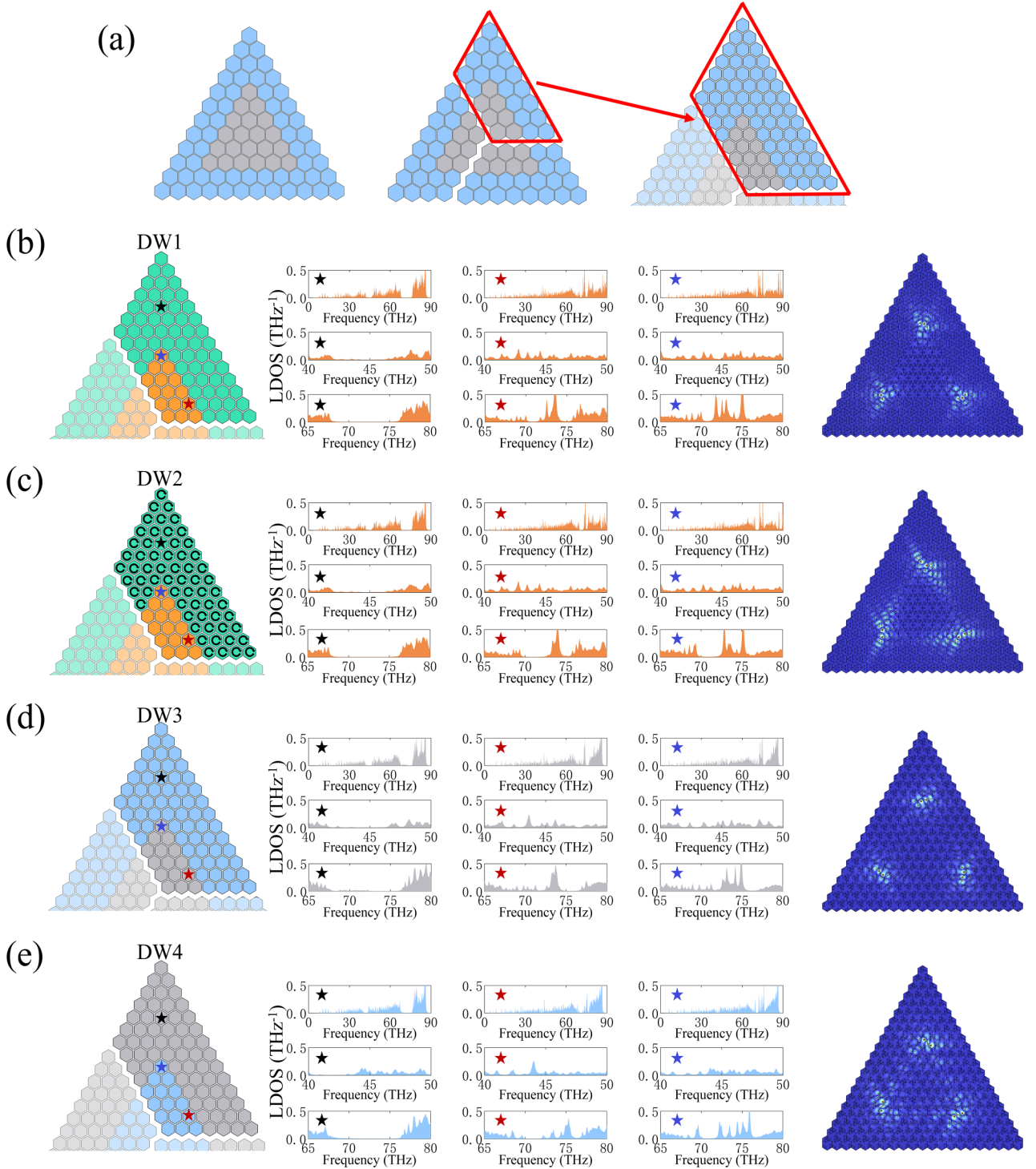


FIG. 10. (a) Simplified schematic of large triangular supercells designed for domain wall (DW) studies, divided into three equivalent areas due to the  $C_3$ -symmetric distribution of mode charge  $C$  throughout the supercell. Research areas are marked with red lines, and actual sections representing one-third of the supercells are also outlined with red lines and indicated by red arrows. The actual supercells are constructed from an interior of 45 unit cells surrounded by four layers of external unit cells, totaling 231 unit cells, with perfect electric conductor (PEC) boundary conditions. (b) and (c) Schematic illustrations of 1 of the 3 equivalent areas of large triangular supercells with DW1 and DW2, where both interiors are type B and the exterior is type A and rotated type A, respectively. Different colored stars indicate unit cells at various boundaries: black for bulk, red for edge, and blue for corner. Photonic local densities of states (LDOSs) for corresponding colored cells are displayed on the right side of the schematic. The photonic LDOSs are segmented into different regions using the same method as shown in Fig. 8(a). On the far right is the calculated electric field ( $E_z$ ) pattern for the corner state of large triangular supercells. (d) and (e) Schematic illustrations of 1 of the 3 equivalent sections of large triangular supercells with DW3 and DW4, with interiors being types E and D, and exteriors being type D and rotated type E, respectively. Stars in the described colors mark the corresponding photonic LDOSs, alongside the electric field ( $E_z$ ) pattern for the corner state.

calculate the mode charge distribution on supercells with DWs in upcoming analyses. In our previous analyses, we simply averaged the Wannier center on the unit cell corner to  $\frac{1}{3}$ , distributing it among the adjacent 2 unit cells. This was based on all bulk polarization  $\mathbf{P}$  is in the dipole phase. However, we need to consider higher-order multipoles, which affect the shape of the Wannier orbitals and cannot be simply represented by dots or circles. This has an impact on the distribution of mode charge at the boundaries, corners, and near-boundary bulk. The effects of these shape variations are discussed in detail in Appendix F in the Supplemental Material [69].

To measure the fractionalization on the four DWs proposed in Sec. III, we constructed a larger triangular supercell, consisting of an inner domain of 45 unit cells surrounded by four layers of other types of unit cells. Given that the mode charge distribution also adheres to  $C_3$  symmetry, we only need to study one-third of the structure, as shown in Fig. 10(a). Similarly, we used black, red, and blue stars to mark unit cells within the bulk, at the edge, and at the corner, respectively. The corresponding LDOS of each unit cell at supercells with DW1, DW2, DW3 (for  $\theta = 17^\circ$ ), and DW4 (for  $\theta = 17^\circ$ ) are displayed in Figs. 10(b)–10(e), along with their respective electric field ( $E_z$ ) patterns for the corner states. In the valley band gap, peaks representing valley TESs appear in the LDOS at the edge of DW3 and DW4, which differ from the PEC boundary conditions. From their respective projected band structures, we know that, in all four cases at the pseudospin gap, there are two gapped TESs, with the lower-frequency TES partially merging into the bulk states, while the higher-frequency TES remains predominantly within the band gap. This is also reflected in the LDOS at the edges. When integrating the LDOS up to the gap between the two TESs, the mode charge of all unit cells is  $\sim 3$ , indicating that the lower-frequency TES originates from the bulk states below the band gap, and the higher-frequency TES from those above. At the corners of the 4 DWs, the peaks representing the corner states vary, and they hybridize with the edge states to different extents. In Appendix G in the Supplemental Material [69], we analyze the LDOS at the edges and corners of DW3 and DW4 under varying  $\theta$  conditions and investigate the LDOS of all unit cells within one-third of a supercell equipped with four DWs in the case of  $\theta = 17^\circ$ .

Our previous mode charge distributions were calculated for the first three bulk states. However, the higher-frequency pseudospin TES originates from the bulk states above the band gap, indicating that the subsequent three bulk states are also topological bands. This leads to the emergence of topological states between the sixth and seventh bands. In Appendix H in the Supplemental Material [69], we present the eigenstate spectrum of the larger triangular supercell with DW3 around the third band gap, calculated at different  $\theta$ . It was found that, as  $\theta$  increases, the topological states located on the DW gradually hybridize with the bulk states, while the topological states on the outer PEC boundaries remain largely unchanged. We chose to analyze the mode charge distribution of the bulk states between the second and third band gaps at  $\theta = 10^\circ$ , where the topological states have not yet hybridized with the 4–6 bulk states. The Wannier bands and Berry curvature for bands 4–6 are like those for bands 1–3, indicating that the configuration of their Wannier centers

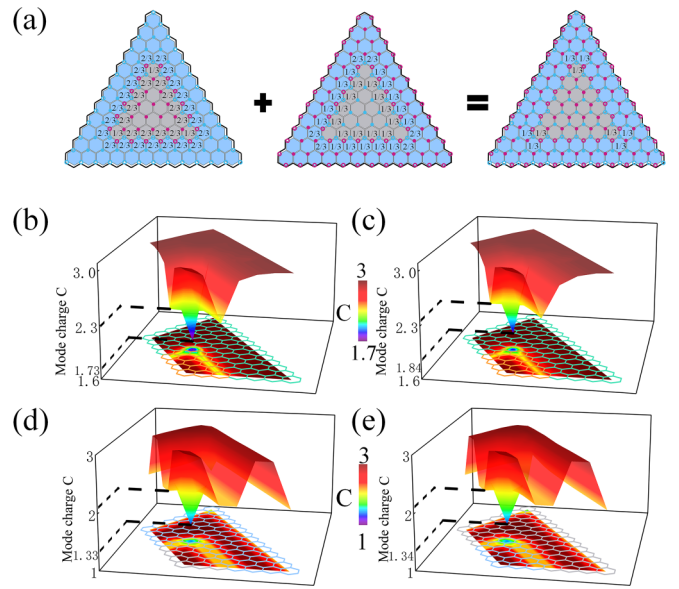


FIG. 11. (a) Distribution and overlay of two noncentral Wannier centers in simplified triangular supercells with DW4. (b) and (c) The distribution map of the mode charge  $C$  for each unit cell in one-third of the large triangular supercells with DW1 and DW2. (d) and (e) The distribution map of the mode charge  $C$  for each unit cell in one-third of the large triangular supercells with DW3 and DW4.

is consistent with what we discussed in Sec. II, with the three Wannier centers located at the maximal Wyckoff positions  $a$ ,  $b$ , and  $c$ , respectively. Figure 11(a) displays the overlay of two noncentral Wannier centers on the DW in simplified triangular supercells with DW4. Adding a centrally located Wannier center, the fractional charges at corners and edges on the DW are the same as previously discussed on PEC, i.e., a fractional corner charge of  $\frac{4}{3}$  (mod 1 results in  $\frac{1}{3}$ ) and an edge charge of 2 (mod 1 results in 0). Unlike the situation with PEC, the external boundaries on the DW relate to the PCs surrounding the inner domain; if the external PC is topological, then the periphery of the DW also possesses topological properties, and if it is trivial, the periphery is also trivial. Figure 11(b) shows the mode charge distribution obtained by integrating the LDOS in one-third of the large triangular supercells with DW1, with a fractional corner charge of 1.73 (mod 1 results in  $0.73 \approx \frac{2}{3}$ ) and an edge charge of 2.3 (mod 1 results in  $0.3 \approx \frac{1}{3}$ ). This distribution is very similar to the mode charge distribution in the large triangular supercells with DW2, as shown in Fig. 11(c). Figures 11(d) and 11(e) display the mode charge distribution at DW3 and DW4, respectively. Notably, the boundaries both inside and outside of their DWs are topological. Compared with DW1 and DW2, they show a potential trend and applications for transitioning from ordinary pseudospin edge states to large-area pseudospin waveguide states. The inconsistency of mode charge at their outermost boundaries with the bulk is due to the surrounding PEC. The calculated fractional corner charges on the DWs are 1.33 and 1.34 (mod 1 results in 0.33 and 0.34,  $\sim \frac{1}{3}$ ), and the fractional edge charges are  $\sim 2.0$  (mod 1 results in 0), consistent with the Wannier center configurations discussed in Fig. 11(a).

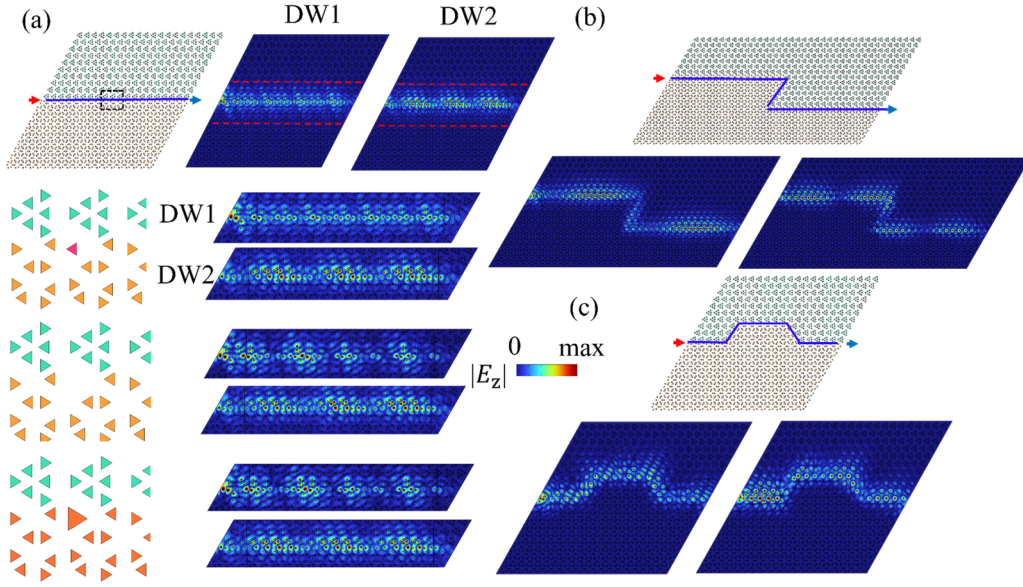


FIG. 12. (a) The light transmission at two domain walls (DWs) with defects. The schematic of the photonic crystal (PC) composed of types A and B PCs, constructing DW2, highlighted by the blue line, is positioned at the top, along with the transmission at two DWs under 73.5 THz. The defects, placed in black dashed rectangles, are amplified. From top to bottom, the defects consist of, in sequence, a  $30^\circ$  rotation of the marked-red Si rod, a cavity, and a larger rod. Corresponding transmissions of these defects between two red dashed lines at two DWs are shown adjacent to them. (b) and (c) The light transmission at various routes. The DW exhibits zigzag interface in (b) and horseshoelike interface in (c). The transmissions at zigzag interfaces (horseshoelike) are illustrated under 69.76 THz (68.5 THz) for DW1 and 69.1 THz (68.5 THz) for DW2.

## V. ROBUSTNESS OF TOPOLOGICAL STATES

The various types of PCs with two DWs are built to demonstrate the robustness of TESs. Figure 12(a) shows PCs with different defects at DWs and the propagation of the light source within the bandwidth of the TES, along with no defect. These defects include the rotation, loss, and alteration in the dimension of 1 of 6 rods in the unit cell. The source at 73.5 THz within the bandwidth of both upper TESs, marked as a red arrow in Fig. 12(a), is selected to investigate the impact of defects on TESs, incidenting from the left. The edge modes are all well located at the interface, and the defects do not significantly affect the topological PCs; this robustness is meaningful in the manufacture and fabrication of optical devices. To further investigate the robustness of TESs, the different routes with turns for two DWs are designed, as displayed in Fig. 12(b) for the zigzag route as well as Fig. 12(c) for the horseshoelike route. The edge modes exhibit similar behavior to the case of defects, remaining well localized at the interface without significant backscattering, even in sharp turns.

Transmittance spectra for DW1 and DW2 with various defects and routes are presented in Fig. 13(a). The transmittances are all  $\sim 1$  within the bandwidth of TESs under any defects and routes. We also observed that these defects caused varying degrees of small transmission loss on the two DWs. Specifically, the rotation defect resulted in  $\sim 0$  dB loss for DW2; the cavity defect caused  $\sim 0.13$  dB loss for DW1 and  $\sim 0.21$  dB loss for DW2; the bigger defect led to  $\sim 0.30$  dB loss for DW1 and  $\sim 0.49$  dB loss for DW2; the zigzag defect caused  $\sim 1.5$  dB loss for DW1 and  $\sim 1.13$  dB loss for DW2. Meanwhile, the difference in TESs between the two DWs appears striking by

the comparison of the two spectra. The bandwidth of TESs at DW1 is consistently wider than that at DW2, and there is some overlap in the frequency of TESs between two DWs.

According to the chirality map, the light sources [ $S_{\pm} = H_0 e^{i\omega t} (\mathbf{e}_x \mp i\mathbf{e}_y)$ ] can be positioned suitably at the DW of PCs. Here,  $S_+$  as a left circularly polarized source can excite pseudospin-up states, and  $S_-$  as a right circularly polarized source can excite pseudospin-down states. Figures 13(b) and 13(c) illustrate the excited state at DW1 under 69.46 THz (at DW2 under 68.89 THz) within the bandwidth of lower TESs. It is conspicuous that the directions of two pseudospin states are opposite at each DW. Moreover, the pseudospin-up state at both DWs propagates to the left, being the same direction of power flow in Fig. 5(d), while the pseudospin-down states propagate to the right. The chirality maps and group velocities of two lower TESs at DWs are similar, leading to the same propagation direction of pseudospin-up (pseudospin-down) states at two DWs. Intriguingly, the chirality maps and group velocities between upper and lower TESs are all opposite, indicating that the propagation direction of pseudospin-up or pseudospin-down states within upper TESs is the same as that within the bandwidth of lower TESs, namely, pseudospin-up toward the left and pseudospin-down toward the right.

## VI. CONCLUSIONS

In conclusion, in this paper, we introduced two pairs of interconvertible DWs constructed using PCs with different higher-order topological phases, leading to the emergence of TESs at the interfaces. On the second pair of interconvertible

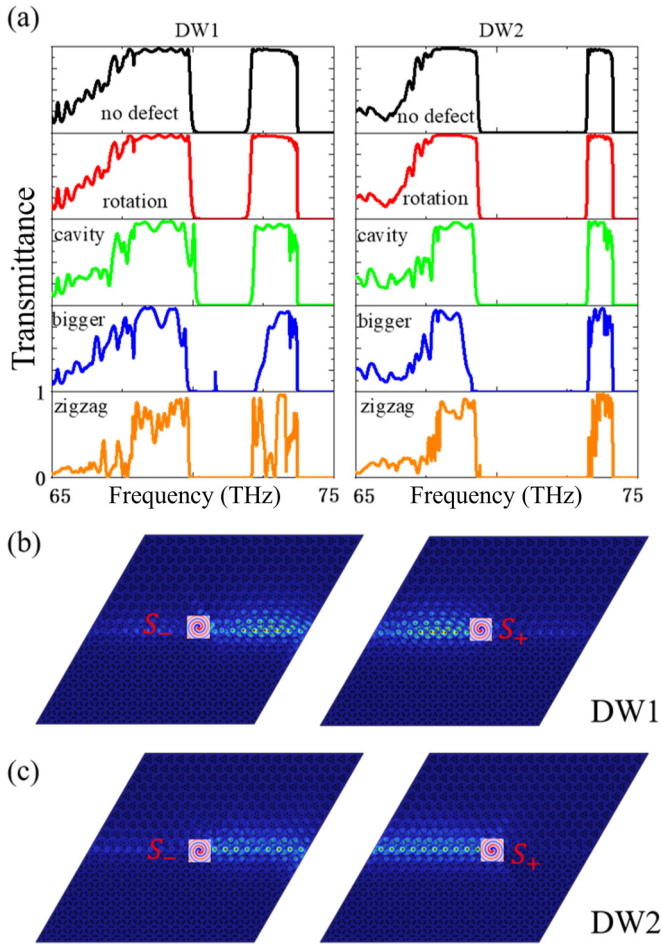


FIG. 13. (a) Transmittance for photonic crystal (PC) slabs with various defects and routes at two domain walls (DWs). (b) and (c) The transmission of  $S_{\pm} = H_0 e^{i\omega t} (\mathbf{e}_x \mp i\mathbf{e}_y)$  as light sources located in the center of DWs. The source  $S_-$  propagates toward the right, and the source  $S_+$  propagates in the opposite direction under 69.1 THz for DW1 and 69.46 THz for DW2.

DWs, valley and pseudospin TESs coexist. We have extensively studied the topological phases of the  $C_3$ -symmetric topological PCs, specifically types B, D, and E. We found that different locations on the DWs, such as the edges and

corners, host rich topological physics compared with the bulk of the system. Using the Wilson loop method, we calculated the Berry curvature distribution and the Wannier band, characterizing the topological nature of types B, D, and E. We confirmed that types D and E belong to different higher-order topological phases by calculating the topological index and the bulk polarization of their first energy bands, determining the distinct positions occupied by their Wannier centers. Interestingly, for types B, D, and E, we calculated the Wannier centers associated with the first three energy bands at maximal Wyckoff positions  $a$ ,  $b$ , and  $c$ . We found that these Wannier centers do not completely deviate from the center of the unit cell like other topological PCs; their Wannier centers only partially deviate. However, only the Wannier centers located at the edge of the unit cell contribute to the filling anomalies at the boundaries and corners. To further validate this partial deviation of Wannier centers, we constructed large triangular supercells with PEC boundaries and integrated the photonic LDOS to calculate the mode charge distribution, which was consistent with our predictions based on Wannier center analysis. This is attributed to the reduction in the symmetry group of the system from  $C_6$  to  $C_3$ . We also calculated the mode charge distribution on the two pairs of DWs and found a wider region of filling anomaly on the second pair. By comparing the photonic LDOS at the corners and edges, we discovered the phenomenon of bulk-edge-corner hybridization. We demonstrated the robustness of TESs by analyzing transmission and transmittance under various routes and defect scenarios, confirming the QSHE in both DWs. We observed significant disparities in TESs and TCSs between the two pairs of interchangeable DWs. Moreover, leveraging the QSHE realized on these DWs and photonic helicity, we designed optical logic gates in the Supplemental Material [69], which extends the applications of topological PCs.

#### ACKNOWLEDGMENTS

We acknowledge the financial support from National Natural Science Foundation of China (NSFC) (Grants No. 62275112, No. 62065007, and No. 11804134) and Natural Science Foundation of Jiangxi Province (Grants No. JXSQ2019201058, No. 09030030, and No. 20232ACB201009).

- [1] M. Z. Hasan and C. L. Kane, Colloquium: Topological insulators, *Rev. Mod. Phys.* **82**, 3045 (2010).
- [2] K. v. Klitzing, G. Dorda, and M. Pepper, New method for high-accuracy determination of the fine-structure constant based on quantized Hall resistance, *Phys. Rev. Lett.* **45**, 494 (1980).
- [3] C. L. Kane and E. J. Mele, Quantum spin Hall effect in graphene, *Phys. Rev. Lett.* **95**, 226801 (2005).
- [4] J.-W. Liu, F.-L. Shi, K. Shen, X.-D. Chen, K. Chen, W.-J. Chen, and J.-W. Dong, Antichiral surface states in time-reversal-invariant photonic semimetals, *Nat. Commun.* **14**, 2027 (2023).
- [5] S. Arora, T. Bauer, N. Parappurath, R. Barczyk, E. Verhagen, and L. Kuipers, Breakdown of spin-to-helicity locking at the

nanoscale in topological photonic crystal edge states, *Phys. Rev. Lett.* **128**, 203903 (2022).

- [6] Q. Pei, H. Yuan, W. Zhang, and X. Zhang, Engineering boundary-dominated topological states in defective hyperbolic lattices, *Phys. Rev. B* **107**, 165145 (2023).
- [7] Y. Wang, H.-X. Wang, L. Liang, W. Zhu, L. Fan, Z.-K. Lin, F. Li, X. Zhang, P.-G. Luan, Y. Poo *et al.*, Hybrid topological photonic crystals, *Nat. Commun.* **14**, 4457 (2023).
- [8] J. Kang, T. Liu, M. Yan, D. Yang, X. Huang, R. Wei, J. Qiu, G. Dong, Z. Yang, and F. Nori, Observation of square-root higher-order topological states in photonic waveguide arrays, *Laser Photonics Rev.* **17**, 2200499 (2023).

- [9] C. A. Rosiek, G. Arregui, A. Vladimirova, M. Albrechtsen, B. Vosoughi Lahijani, R. E. Christiansen, and S. Stobbe, Observation of strong backscattering in valley-Hall photonic topological interface modes, *Nat. Photonics* **17**, 386 (2023).
- [10] X. Yin, J. Jin, M. Soljačić, C. Peng, and B. Zhen, Observation of topologically enabled unidirectional guided resonances, *Nature (London)* **580**, 467 (2020).
- [11] Z.-X. Gao, J.-Z. Liao, F.-L. Shi, K. Shen, F. Ma, M. Chen, X.-D. Chen, and J.-W. Dong, Observation of unidirectional bulk modes and robust edge modes in triangular photonic crystals, *Laser Photonics Rev.* **17**, 2201026 (2023).
- [12] B. Yan, Y. Peng, A. Shi, J. Xie, P. Peng, and J. Liu, Pseudo-spin-valley coupled topological states protected by different symmetries in photonic crystals, *Opt. Lett.* **47**, 2044 (2022).
- [13] A. V. Poshakinskiy, A. N. Poddubny, L. Pilozzi, and E. L. Ivchenko, Radiative topological states in resonant photonic crystals, *Phys. Rev. Lett.* **112**, 107403 (2014).
- [14] B. Yang, Q. Guo, D. Wang, H. Wang, L. Xia, W. Xu, M. Kang, R.-Y. Zhang, Z.-Q. Zhang, Z. Zhu *et al.*, Scalar topological photonic nested meta-crystals and skyrmion surface states in the light cone continuum, *Nat. Mater.* **22**, 1203 (2023).
- [15] L.-H. Wu and X. Hu, Scheme for achieving a topological photonic crystal by using dielectric material, *Phys. Rev. Lett.* **114**, 223901 (2015).
- [16] G. Hu, Q. Ou, G. Si, Y. Wu, J. Wu, Z. Dai, A. Krasnok, Y. Mazon, Q. Zhang, Q. Bao *et al.*, Topological polaritons and photonic magic angles in twisted  $\alpha$ -MoO<sub>3</sub> bilayers, *Nature (London)* **582**, 209 (2020).
- [17] J. Jin, X. Yin, L. Ni, M. Soljačić, B. Zhen, and C. Peng, Topologically enabled ultrahigh- $Q$  guided resonances robust to out-of-plane scattering, *Nature (London)* **574**, 501 (2019).
- [18] S. Zanotti, H. S. Nguyen, M. Minkov, L. C. Andreani, and D. Gerace, Theory of photonic crystal polaritons in periodically patterned multilayer waveguides, *Phys. Rev. B* **106**, 115424 (2022).
- [19] C. Jiang, Y. Song, X. Li, P. Lu, and S. Ke, Photonic Möbius topological insulator from projective symmetry in multi-orbital waveguides, *Opt. Lett.* **48**, 2337 (2023).
- [20] Y. Ke, J. Huang, W. Liu, Y. Kivshar, and C. Lee, Topological inverse band theory in waveguide quantum electrodynamics, *Phys. Rev. Lett.* **131**, 103604 (2023).
- [21] E. Thareja and I. Vekhter, Bound states and controllable currents on topological insulator surfaces with extended magnetic defects, *Phys. Rev. B* **107**, 144205 (2023).
- [22] Z. Zhang, Z. Lan, Y. Xie, M. L. N. Chen, W. E. I. Sha, and Y. Xu, Bound topological edge state in the continuum for all-dielectric photonic crystals, *Phys. Rev. Appl.* **16**, 064036 (2021).
- [23] T. Feng, Y. Xu, W. Zhang, and A. E. Miroschnichenko, Ideal magnetic dipole scattering, *Phys. Rev. Lett.* **118**, 173901 (2017).
- [24] L. Lin, S. Kruk, Y. Ke, C. Lee, and Y. Kivshar, Topological states in disordered arrays of dielectric nanoparticles, *Phys. Rev. Res.* **2**, 043233 (2020).
- [25] S. Yu, C.-W. Qiu, Y. Chong, S. Torquato, and N. Park, Engineered disorder in photonics, *Nat. Rev. Mater.* **6**, 226 (2021).
- [26] X. Cheng, T. Qu, L. Xiao, S. Jia, J. Chen, and L. Zhang, Topological Anderson amorphous insulator, *Phys. Rev. B* **108**, L081110 (2023).
- [27] J. Fan, Z. Sun, Y. Lu, W. Luo, M. Ren, W. Cai, and J. Xu, Topological super-modes engineering with acoustic graphene plasmons, *Opt. Express* **31**, 3698 (2023).
- [28] G. Xu, X. Zhou, S. Yang, J. Wu, and C.-W. Qiu, Observation of bulk quadrupole in topological heat transport, *Nat. Commun.* **14**, 3252 (2023).
- [29] R. Colom, E. Mikheeva, K. Achouri, J. Zuniga-Perez, N. Bonod, O. J. F. Martin, S. Burger, and P. Genevet, Crossing of the branch cut: The topological origin of a universal  $2\pi$ -phase retardation in non-Hermitian metasurfaces, *Laser Photonics Rev.* **17**, 2200976 (2023).
- [30] Z. Sakotic, P. Stankovic, V. Bengin, A. Krasnok, A. Alú, and N. Jankovic, Non-Hermitian control of topological scattering singularities emerging from bound states in the continuum, *Laser Photonics Rev.* **17**, 2200308 (2023).
- [31] L. Zhang, X.-M. Wang, X.-M. Qiu, Z. Wang, and J.-Y. Yan, Light controlled topological plasmonics in a graphene lattice arrayed by metal nanoparticles, *Phys. Rev. B* **108**, 085402 (2023).
- [32] S.-X. Xia, D. Zhang, Z. Zheng, X. Zhai, H. Li, J.-Q. Liu, L.-L. Wang, and S.-C. Wen, Topological plasmons in stacked graphene nanoribbons, *Opt. Lett.* **48**, 644 (2023).
- [33] Y. Sheffer, R. Queiroz, and A. Stern, Symmetries as the guiding principle for flattening bands of Dirac fermions, *Phys. Rev. X* **13**, 021012 (2023).
- [34] M. Makwana, R. Craster, and S. Guenneau, Topological beam-splitting in photonic crystals, *Opt. Express* **27**, 16088 (2019).
- [35] B. Xie, H.-X. Wang, X. Zhang, P. Zhan, J.-H. Jiang, M. Lu, and Y. Chen, Higher-order band topology, *Nat. Rev. Phys.* **3**, 520 (2021).
- [36] L. Lu, J. D. Joannopoulos, and M. Soljačić, Topological photonics, *Nat. Photonics* **8**, 821 (2014).
- [37] S. Yan, J. Yang, S. Shi, Z. Zuo, C. Wang, and X. Xu, Transport of a topologically protected photonic waveguide on-chip, *Photon. Res.* **11**, 1021 (2023).
- [38] G. Arregui, J. Gomis-Bresco, C. M. Sotomayor-Torres, and P. D. Garcia, Quantifying the robustness of topological slow light, *Phys. Rev. Lett.* **126**, 027403 (2021).
- [39] X. Cheng, C. Jouvaud, X. Ni, S. H. Mousavi, A. Z. Genack, and A. B. Khanikaev, Robust reconfigurable electromagnetic pathways within a photonic topological insulator, *Nat. Mater.* **15**, 542 (2016).
- [40] Y. Yang, Y. F. Xu, T. Xu, H.-X. Wang, J.-H. Jiang, X. Hu, and Z. H. Hang, Visualization of a unidirectional electromagnetic waveguide using topological photonic crystals made of dielectric materials, *Phys. Rev. Lett.* **120**, 217401 (2018).
- [41] T. Ma, A. B. Khanikaev, S. H. Mousavi, and G. Shvets, Guiding electromagnetic waves around sharp corners: Topologically protected photonic transport in metawaveguides, *Phys. Rev. Lett.* **114**, 127401 (2015).
- [42] T. Ma and G. Shvets, All-Si valley-Hall photonic topological insulator, *New J. Phys.* **18**, 025012 (2016).
- [43] X.-T. He, E.-T. Liang, J.-J. Yuan, H.-Y. Qiu, X.-D. Chen, F.-L. Zhao, and J.-W. Dong, A silicon-on-insulator slab for topological valley transport, *Nat. Commun.* **10**, 872 (2019).
- [44] M. I. Shalaev, W. Walasik, A. Tsukernik, Y. Xu, and N. M. Litchinitser, Robust topologically protected transport in photonic crystals at telecommunication wavelengths, *Nat. Nanotechnol.* **14**, 31 (2019).

- [45] S. Xu, Y. Wang, and R. Agarwal, Absence of topological protection of the interface states in  $\mathbb{Z}_2$  photonic crystals, *Phys. Rev. Lett.* **131**, 053802 (2023).
- [46] K. Peng, W. Li, M. Sun, J. D. H. Rivero, C. Ti, X. Han, L. Ge, L. Yang, X. Zhang, and W. Bao, Topological valley Hall polariton condensation, *Nat. Nanotechnol.* (2024), doi:10.1038/s41565-024-01674-6.
- [47] Y. Kawaguchi, D. Smirnova, F. Komissarenko, S. Kiriushechkina, A. Vakulenko, M. Li, A. Alù, and A. B. Khanikaev, Pseudo-spin switches and Aharonov-Bohm effect for topological boundary modes, *Sci. Adv.* **10**, eadn6095 (2024).
- [48] L. He, D. Liu, H. Zhang, F. Zhang, W. Zhang, X. Feng, Y. Huang, K. Cui, F. Liu, W. Zhang, and X. Zhang, Topologically protected quantum logic gates with valley-Hall photonic crystals, *Adv. Mater.* **36**, 2311611 (2024).
- [49] X.-D. Chen, W.-M. Deng, F.-L. Shi, F.-L. Zhao, M. Chen, and J.-W. Dong, Direct observation of corner states in second-order topological photonic crystal slabs, *Phys. Rev. Lett.* **122**, 233902 (2019).
- [50] Y. Peng, E. Liu, B. Yan, J. Xie, A. Shi, P. Peng, H. Li, and J. Liu, Higher-order topological states in two-dimensional Stampfli-triangle photonic crystals, *Opt. Lett.* **47**, 3011 (2022).
- [51] Y. Zhang, D. Bongiovanni, Z. Wang, X. Wang, S. Xia, Z. Hu, D. Song, D. Jukić, J. Xu, R. Morandotti, H. Buljan, and Z. Chen, Realization of photonic  $p$ -orbital higher-order topological insulators, *Elight* **3**, 5 (2023).
- [52] B.-Y. Xie, G.-X. Su, H.-F. Wang, H. Su, X.-P. Shen, P. Zhan, M.-H. Lu, Z.-L. Wang, and Y.-F. Chen, Visualization of higher-order topological insulating phases in two-dimensional dielectric photonic crystals, *Phys. Rev. Lett.* **122**, 233903 (2019).
- [53] L. Lei, S. Xiao, W. Liu, Q. Liao, L. He, and T. Yu, Polarization-independent second-order photonic topological corner states, *Phys. Rev. Appl.* **20**, 024014 (2023).
- [54] K.-H. Kim and K.-K. Om, Multiband photonic topological valley-hall edge modes and second-order corner states in square lattices, *Adv. Opt. Mater.* **9**, 2001865 (2021).
- [55] B.-Y. Xie, H.-F. Wang, H.-X. Wang, X.-Y. Zhu, J.-H. Jiang, M.-H. Lu, and Y.-F. Chen, Second-order photonic topological insulator with corner states, *Phys. Rev. B* **98**, 205147 (2018).
- [56] M. Proctor, P. A. Huidobro, B. Bradlyn, M. B. de Paz, M. G. Vergniory, D. Bercioux, and A. García-Etxarri, Robustness of topological corner modes in photonic crystals, *Phys. Rev. Res.* **2**, 042038(R) (2020).
- [57] H.-R. Kim, M.-S. Hwang, D. Smirnova, K.-Y. Jeong, Y. Kivshar, and H.-G. Park, Multipolar lasing modes from topological corner states, *Nat. Commun.* **11**, 5758 (2020).
- [58] K.-H. O and K.-H. Kim, Ultrahigh- $Q$  Fano resonance using topological corner modes in second-order pseudospin-Hall photonic systems, *Opt. Laser Technol.* **147**, 107616 (2022).
- [59] A. Cerjan, M. Jürgensen, W. A. Benalcazar, S. Mukherjee, and M. C. Rechtsman, Observation of a higher-order topological bound state in the continuum, *Phys. Rev. Lett.* **125**, 213901 (2020).
- [60] Z.-K. Lin, Y. Wu, B. Jiang, Y. Liu, S.-Q. Wu, F. Li, and J.-H. Jiang, Topological Wannier cycles induced by sub-unit-cell artificial gauge flux in a sonic crystal, *Nat. Mater.* **21**, 430 (2022).
- [61] T. Li, P. Zhu, W. A. Benalcazar, and T. L. Hughes, Fractional disclination charge in two-dimensional  $C_n$ -symmetric topological crystalline insulators, *Phys. Rev. B* **101**, 115115 (2020).
- [62] W. A. Benalcazar, T. Li, and T. L. Hughes, Quantization of fractional corner charge in  $C_n$ -symmetric higher-order topological crystalline insulators, *Phys. Rev. B* **99**, 245151 (2019).
- [63] C.-P. Liang, Y. Liu, F.-F. Li, S.-W. Leung, Y. Poo, and J.-H. Jiang, Fractional topological numbers at photonic edges and corners, *Phys. Rev. Appl.* **20**, 034028 (2023).
- [64] Y. Liu, S. Leung, F.-F. Li, Z.-K. Lin, X. Tao, Y. Poo, and J.-H. Jiang, Bulk-disclination correspondence in topological crystalline insulators, *Nature (London)* **589**, 381 (2021).
- [65] C. W. Peterson, T. Li, W. A. Benalcazar, T. L. Hughes, and G. Bahl, A fractional corner anomaly reveals higher-order topology, *Science* **368**, 1114 (2020).
- [66] M. C. Rechtsman, Y. Plotnik, J. M. Zeuner, D. Song, Z. Chen, A. Szameit, and M. Segev, Topological creation and destruction of edge states in photonic graphene, *Phys. Rev. Lett.* **111**, 103901 (2013).
- [67] M. Bellec, U. Kuhl, G. Montambaux, and F. Mortessagne, Manipulation of edge states in microwave artificial graphene, *New J. Phys.* **16**, 113023 (2014).
- [68] D. Song, V. Paltoglou, S. Liu, Y. Zhu, D. Gallardo, L. Tang, J. Xu, M. Ablowitz, N. K. Efremidis, and Z. Chen, Unveiling pseudospin and angular momentum in photonic graphene, *Nat. Commun.* **6**, 6272 (2015).
- [69] See Supplemental Material at <http://link.aps.org/supplemental/10.1103/PhysRevB.110.075407> for details, including Appendix A: The Berry curvature and Wannier band; Appendix B: The projected bands at different  $\theta$  and optical logic gates; Appendix C: Photonic LDOS and mode charges; Appendix D: The robustness of mode charges obtained from the LDOS; Appendix E: Photonic LDOS of PEC edge and PEC corner at different  $\theta$ ; Appendix G: Photonic LDOS of edge and corner at DW3 and DW4 for different  $\theta$ ; and Appendix H: Third topological band gap at DW3 and DW4, which includes Refs. [62,70–76].
- [70] T. Fukui, Y. Hatsugai, and H. Suzuki, Chern numbers in discretized Brillouin zone: Efficient method of computing (spin) Hall conductances, *J. Phys. Soc. Jpn.* **74**, 1674 (2005).
- [71] R. D. King-Smith and D. Vanderbilt, Theory of polarization of crystalline solids, *Phys. Rev. B* **47**, 1651 (1993).
- [72] W. A. Benalcazar, B. A. Bernevig, and T. L. Hughes, Electric multipole moments, topological multipole moment pumping, and chiral hinge states in crystalline insulators, *Phys. Rev. B* **96**, 245115 (2017).
- [73] W. A. Benalcazar, B. A. Bernevig, and T. L. Hughes, Quantized electric multipole insulators, *Science* **357**, 61 (2017).
- [74] E. Palmerduca and H. Qin, Photon topology, *Phys. Rev. D* **109**, 085005 (2024).
- [75] Z. Lan, Y. Chen, L. An, and Z. Su, Chern, dipole, and quadrupole topological phases of a simple magneto-optical photonic crystal with a square lattice and an unconventional unit cell, *Phys. Rev. B* **109**, 045402 (2024).
- [76] Z. Lan, Y. Chen, J. Zhu, and Z. Su, Quadrupole topological phases and filling anomaly in all-dielectric Lieb lattice photonic crystals, *Opt. Lett.* **48**, 5747 (2023).
- [77] Z. Lan, M. L. N. Chen, J. W. You, and W. E. I. Sha, Large-area quantum-spin-Hall waveguide states in a three-layer topological

- photonic crystal heterostructure, [Phys. Rev. A \*\*107\*\*, L041501 \(2023\)](#).
- [78] Z. Lan, J. W. You, Q. Ren, W. E. I. Sha, and N. C. Panoiu, Second-harmonic generation via double topological valley-Hall kink modes in all-dielectric photonic crystals, [Phys. Rev. A \*\*103\*\*, L041502 \(2021\)](#).
- [79] T. Zheng, K. Hu, Y. Zhou, C. Xu, and M.-H. Lu, Fractional mode charge in  $C_n$ -symmetric higher-order topological crystalline insulators, [J. Appl. Phys. \*\*134\*\*, 034502 \(2023\)](#).
- [80] W. A. Benalcazar and A. Cerjan, Bound states in the continuum of higher-order topological insulators, [Phys. Rev. B \*\*101\*\*, 161116\(R\) \(2020\)](#).